FY 2021 DOCTRAL THESIS

Multiwavelength study of energy injections into the hotspot from the active galactic nucleus jet

(多波長観測による活動銀河核ジェットから ホットスポットへのエネルギー供給の研究)

Author Yuji Sunada
Student Number 19DS006

Supervisor Yukikatsu Terada

Graduate School of Science and Engineering
Saitama University

December 7, 2021

Contents

Chapter 1.

Introduction

The bright region called "hot spot" is observed at the terminal of the relativistic jets in Fanaroff-Riley type-II (FR-II, Fanaroff1974) radio galaxy. In the general picture, the jets form a terminal shock and convert their kinetic energy into particle acceleration via the shock. The hot spots are the sites where the accelerated particles radiate. Their emission in radio to near-infrared/optical band is well explained as the synchrotron emission from the accelerated electrons (e.g., Meisenheimer et al. (1989, 1997); Mack et al. (2009); Werner et al. (2012)). On the other hand, the X-ray spectrum is brighter and harder than the extrapolation of the low-energy component (e.g., Harris et al. (1994); Wilson et al. (2000)), and then the one-zone Synchrotron-Self-Compton (SSC) process is taken into account. The SSC scenario well explains the X-ray spectrum of high-radio-power hot spot (e.g., Harris et al. (2000); Hardcastle et al. (2004); Kataoka and Stawarz (2005); Stawarz et al. (2007); Werner et al. (2012)). However, for the low-power ones, the SSC X-ray scenario requires a significantly lower magnetic field strength than that estimated under the energy equipartition condition (e.g., Wilson et al. (2001); Hardcastle et al. (2004); Kataoka and Stawarz (2005)). Moreover, there are spatial difference between the radio and X-ray emission regions (e.g.,Thimmappa et al. (2020); Orienti et al. (2020); Migliori et al. (2020)). Therefore the SSC scenario is denied, and as the alternative process, the synchrotron radiation of another electron population is considered plausible X-ray origin (e.g., Hardcastle et al. (2004)).

The X-ray synchrotron emission corresponds to the high energy electrons with typicall 10–100 TeV. In addition, by considering the radiative lifetime of the electrons of an order of 10 years, the X-ray reflects the recent particle acceleration. Thus, X-ray observations are important to study particle acceleration in the hot spots. The radio loudness is probably related to the magnetic field intensity and the magnetic field is expected as the cause of the different X-ray origin. However, to estimate the magnetic field is difficult and the cause is still unclear. In this paper, I investigate the magnetic field and X-ray origin of the representative hotspots, which are hosted by Cygnus A and Pictor A.

Chapter 2.

Energy flow in radio galaxy

Active lactic nucleus (AGN) is a bright source located in the central region of the galaxy. The AGNs exbit a variety of spectral and morphological features. Then, AGNs are firstly classified by their luminosities and radio loudness. The AGN with high luminosity ($\gtrsim 10^{12} L_{\odot}$) and high/low radio one is called radio loud/quiet quasi stellar object (quasar). The middle luminosity ($10^{10} - 10^{11} L_{\odot}$) AGN with high radio loudness is called radio galaxy and with low radio loudness called Seytfert type galaxy. The radio galaxies clearly show the bipolar jets and are suitable objects to investigate the jet. The radio galaxies are divided into two types of FR-I and FR-II radio galaxy (Fanaroff and Riley 1974). Figure 2 shows typical FR-I and -II Radio galaxies. The FR-II have tightly collimated and jet with faint emission and bright region of hotspot at the jet termination region. This indicates that in FR-II radio galaxy, the jet loss most of their bulk energy at the termination region. Therefore the hotspot of FR-II radio galaxy have the total energy of the jet. In following sections, I explain about the structure in FR-II radio galaxy.

2.1 nucleus

The nucleus is the super massive black hole with the mass of typically $10^6 - 10^{11}\ M_{\odot}$. The black holes attract the surrounding gases and release the gravitational energies. In this time, a part of the energy and the gas are ejected from the nucleus to the intergalactic space as the jet.

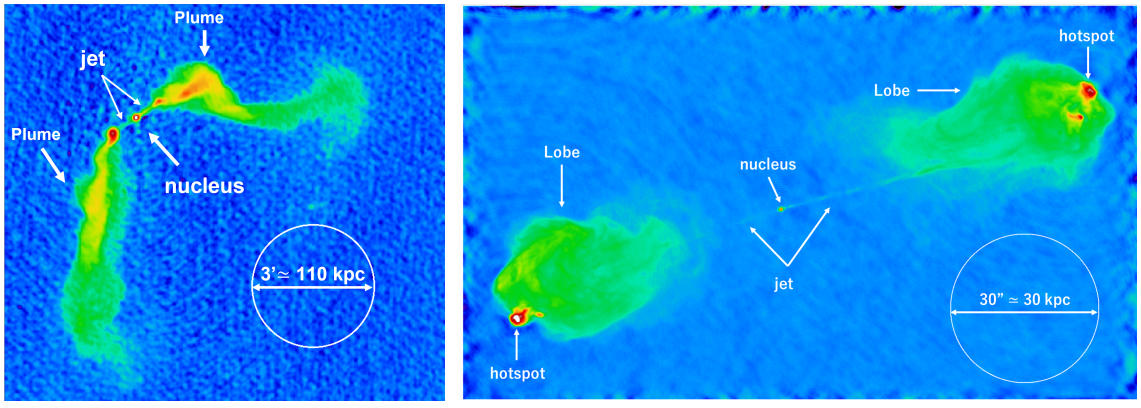

Figure2.1 The FR-I and FR-II radio galaxies of 3C465 and Cygnus A are shown in left and right panels, respectively.

2.2 jet

The jet is the plasma launched from the nucleus and proceeding to the inter galactic space. The long-term monitoring observation of the jet directly measured advance velocity of the jet and discovered the superluminal motion. This is the evidence of the relativistic velocity of the jet.

2.3 hot spot

The hotspot is the bright region at the terminal of the jet. In the general picture, the hotspot is the site where the jet disperse their kinetic energy and convert it to the particle acceleration and magnetic field amplification. The accelerated particles emit by the interaction of the amplificated magnetic field via the synchrotron process. Because the energy of the radiation is derived from the jet kinetic energy through the particle and magnetic field energy, it can be thought of as the visualization of jet energy in hotspots.

2.4 lobe

The lobe is the most extended structure in FR-II radio galaxy. The lobe is considered to be fulfilled by the plasma flowed out from the hotspot. Therefore the lobes have the history of the hotspot.

Chapter 3.

Broadband radiation of hot spots

3.1 Radiative process of the hot spot

3.1.1 Synchrotron radiation

From a basic electronmagnetic theory, moving charged particles have radiation when their trajectory is bend by any external force. In astrophysical environments, the magnetic field, which cause the charge of the particle trajectory is immutably exists. Thus, the radiation, called "synchrotron" is caused by the interaction between the magnetic field and the electrons.

At first, we describes the synchrotron power from single electron as,

$$P_{\rm syn} = \frac{2q^4 B^2 E_{\rm e}^2 \sin^2\alpha}{3m_{\rm e}^4 c^5}. \tag{3.1}$$

The synchrotron radiation has a higher power in higher electron energy and higher magnetic field.

The synchrotron process creates a broadband spectrum even from a monochromatic energy electron. The spectrum emittied from single monochromatic energy electron is obtained as

$$\left(\frac{{\rm d}N_\gamma}{{\rm d}E_\gamma {\rm d}t}\right)_{\rm single} = \frac{\sqrt{3}q^3 B\sin\alpha}{hmc^2 E_\gamma} F\left(\frac{E_\gamma}{E_{\rm cr}}\right) \tag{3.2}$$

$$F(x) \equiv x\int_x^\infty K_{5/3}(\xi){\rm d}\xi \tag{3.3}$$

$$E_{\rm cr} = \frac{3hq{E_{\rm e}}^2 B\sin\alpha}{4\pi {m_{\rm e}}^3 c^5} \simeq 1.1\times\left(\frac{E_\gamma}{1\ {\rm TeV}}\right)^2\left(\frac{B}{100\ \mu{\rm G}}\right)\left(\frac{\sin\alpha}{1}\right){\rm eV} \tag{3.4}$$

Here, $K_{5/3}$ is a modified Bessel function with an order of $5/3$. $E_{\rm cr}$ is a synchrotron critical energy. The synchrotron spectrum shpae is defined as the function of $F(x)$. Figure 3.1.1 shows a $F(x)$. The function reaches a maximum value at x $\simeq$ 0.29 and steeply decrease above. Thus, the synchrotron emission concentrates around the critical energy.

To integrate the spectrum over the photon energy, the synchrotron power from the songle electron is derived as,

In the astrophysical enviorment where synchrotron radiation plays important role, the electron distributes broadband energy. The synchrotron spectrum from any electron distribution is derived from a convolution of the electron energy spectrum and the monochromatic synchrotron spectrum as

$$\frac{{\rm d}N_\gamma}{{\rm d}E_\gamma {\rm d}t} = \int_{E_{\rm e,min}}^{E_{\rm e,max}} \frac{{\rm d}N_{\rm e}}{{\rm d}E_{\rm e}} \times \left(\frac{{\rm d}N_\gamma}{{\rm d}E_\gamma {\rm d}t}\right)_{\rm single} {\rm d}E_{\rm e}. \tag{3.5}$$

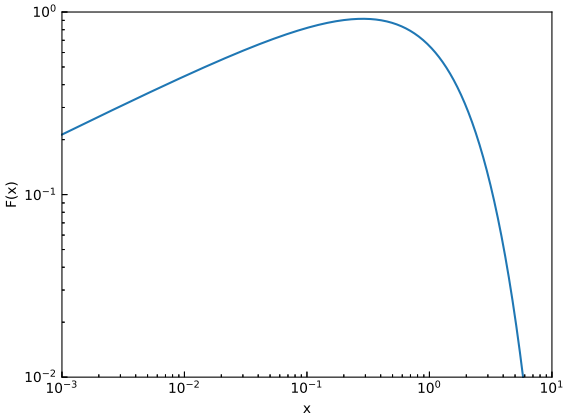

Figure3.1 The function of $F(x)$

To see an outline of the spectrum, approximating that synchrotron emission has the monochromatic spectrum concentrating on the critical energy as

$$\left(\frac{\mathrm{d}N_\gamma}{\mathrm{d}E_\gamma \mathrm{d}t}\right)_{\mathrm{single}} \approx \delta(E_\gamma - E_{\mathrm{cr}}) \times \int_0^\infty \left(\frac{\mathrm{d}N_\gamma}{\mathrm{d}E_\gamma \mathrm{d}t}\right)_{\mathrm{single}} \mathrm{d}E_\gamma \tag{3.6}$$

$$\propto \delta(E_\gamma - E_{\mathrm{cr}}) \times \int_0^\infty \frac{1}{E_\gamma} F\left(\frac{E_\gamma}{E_{\mathrm{cr}}}\right) \mathrm{d}E_\gamma, \tag{3.7}$$

and here,

$$\int_0^\infty \frac{1}{E_\gamma} F\left(\frac{E_\gamma}{E_{\mathrm{cr}}}\right) \mathrm{d}E_\gamma = \int_0^\infty xF(x)dx = \text{constant}. \tag{3.8}$$

Therefore,

$$\left(\frac{\mathrm{d}N_\gamma}{\mathrm{d}E_\gamma \mathrm{d}t}\right)_{\mathrm{single}} \propto \delta(E_\gamma - E_{\mathrm{cr}}). \tag{3.9}$$

By adopting the power-law electron distribution of

$$\frac{\mathrm{d}N_{\mathrm{e}}}{\mathrm{d}E_{\mathrm{e}}} \propto E_{\mathrm{e}}^{-p}, \tag{3.10}$$

and the equation 3.5 is described as

$$\frac{\mathrm{d}N_\gamma}{\mathrm{d}E_\gamma \mathrm{d}t} \propto \int_{E_{\mathrm{e,min}}}^{E_{\mathrm{e,max}}} E_{\mathrm{e}}^{-p} \delta(E_\gamma - E_{\mathrm{cr}}) \mathrm{d}E_{\mathrm{e}} \tag{3.11}$$

$$\propto \int_{E_{\mathrm{cr,min}}}^{E_{\mathrm{cr,max}}} E_{\mathrm{cr}}^{-\frac{p+1}{2}} \delta(E_\gamma - E_{\mathrm{cr}}) \mathrm{d}E_{\mathrm{cr}} \tag{3.12}$$

$$\propto E_\gamma^{-\frac{p+1}{2}}. \tag{3.13}$$

Therefore, the energy index of the power-law distribution electrons of p is obtained from the photon index of the synchrotron spectrum of Γ as $p = 2\Gamma - 1$.

3.1.2 Inverse Compton scattering

When photons interact with electrons, the photon energies are transferred to the electrons. Such interaction is inelastic scattering called Compton scattering. The scattering cross-sectioin when the electron is in stationary, is given from Klein-Nishina's formula. The case of moving-electron, especially in relativistic regime, the interaction is called "Inverse Compton" (IC) scattering calculated by considering the change of the frames. In the IC scattering, the electrons transfer their energy to the seed photons and then it is treated as the emission process of the electrons. The power of the IC scattering is written as,

$$P_{\rm IC} = \frac{4}{3}\sigma_{\rm T} c \gamma^2 \beta^2 U_{\rm ph} \tag{3.14}$$

The typical energy of the emitted photons is $E_{\gamma,\rm IC} = \gamma^2 E_{\gamma,\rm seed}$. The dependences of the power and emitted photon energy to the electron energy are same as the synchrotron emission, and then, the energy index relation between the electrons and emitted photons is also same as synchrotron emission.

3.2 Spectral energy distribution of hot spots

3.2.1 Synchrotron spectrum with radiative cooling

The synchrotron emitting electron suffer from radiative cooling and lose their own energy. The time development of the electron energy is culculated as

$$\frac{{\rm d}E_{\rm e}(t)}{{\rm d}t} = -P_{\rm syn} \tag{3.15}$$

$$= -\frac{2q^4 B^2 \sin^2\alpha}{3m_{\rm e}^4 c^5} E_{\rm e}(t)^2 \equiv -A E_{\rm e}(t)^2. \tag{3.16}$$

Then,

$$\int \frac{{\rm d}E_{\rm e}}{E_{\rm e}(t)^2} = -A \int {\rm d}t \tag{3.17}$$

$$E_{\rm e}(t) = \frac{1}{At + C}. \tag{3.18}$$

Here, C is an integration constant. And, $E_{\rm e}(0) = E_{\rm e,0}$, and hence $C = 1/E_{\rm e,0}$. Therefore, finally,

$$E_{\rm e}(t) = \frac{1}{AE_{\rm e,0}t + 1} \tag{3.19}$$

$$= \frac{E_{\rm e,0}}{1 + t/(A/E_{\rm e,0})} \tag{3.20}$$

$$= \frac{E_{\rm e,0}}{t/\tau_{\rm syn} + 1} \tag{3.21}$$

$$\tau_{\rm syn} \equiv \frac{-1}{AE_{\rm e,0}} = \frac{3m_{\rm e}^4 c^5}{2q^4 \sin^2\alpha} B^{-2} E_{\rm e,0}^{-1}. \tag{3.22}$$

Figure 3.2.1 shows the development of electron energy. The electron lose the energy in synchrotron radiative cooling time scale of $\tau_{\rm syn}$. The radiative cooling plays important role in astropysical context. The cooling time is shorter for higher energy electrons. This means that the electrons with the highest energy lose energy at first.

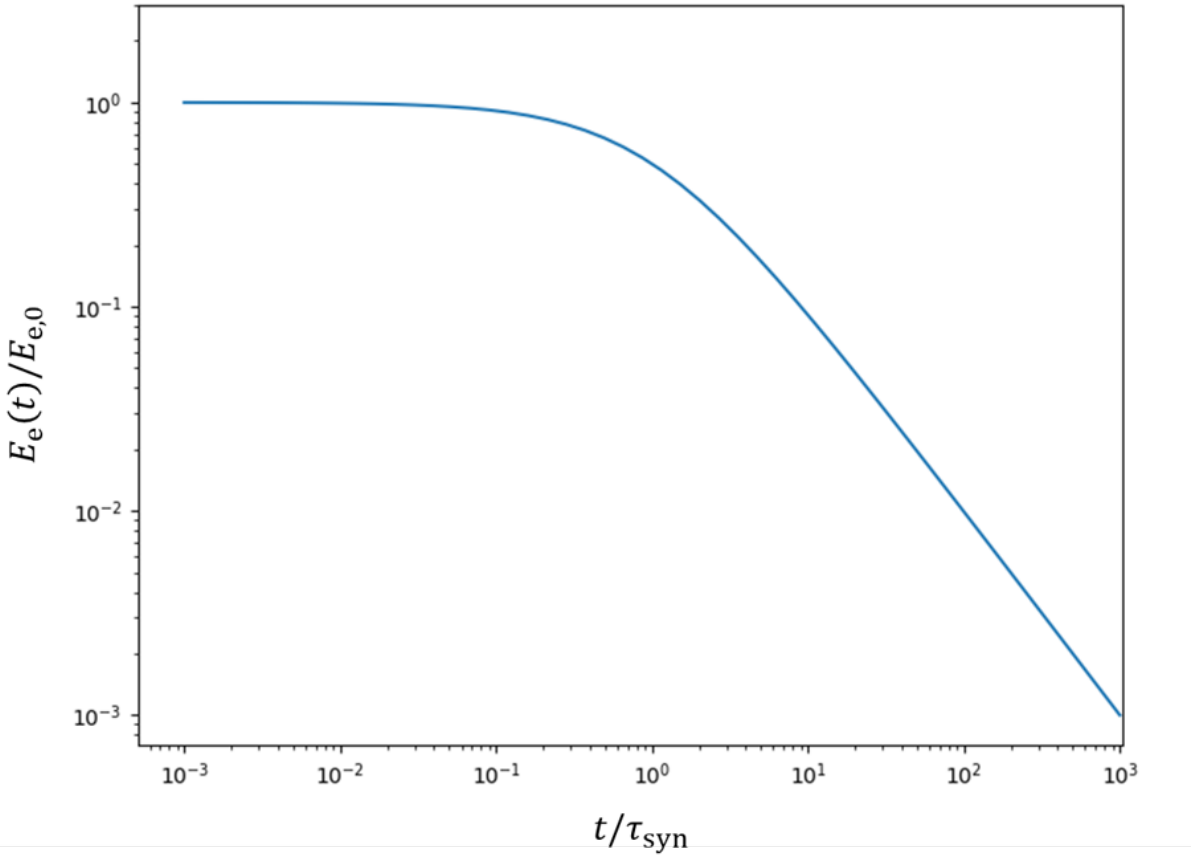

Figure3.2 The time development of electron energy under the synchrotron radiative cooling.

Therefore, the electron population under the radiative cooling have the maximum energy depending on the time. The maximum energy at a time of t later is obtained by equalizing the time ans the cooling time as

$$t = \tau_{\rm syn} \tag{3.23}$$

$$E_{\rm e,max}(t) = \frac{3m_{\rm e}^4c^5}{2q^4\sin^2\alpha}B^{-2}t^{-1}. \tag{3.24}$$

3.2.2 SSC process and energetics

In the synchrotron emitting sources, there are relativistic electrons and synchrotron photons. Therefore, the IC scattering of the electrons by using thesynchrotron photons as the seed ones is naturally occurs. This is called "Synchrotron-Self-Compton" (SSC) process. The synchrotron luminosity depends on the electron and magnetic field energy densities, on the other hand, the IC scattering luminosity depends on the electron and photon energy densities. Because the photon energy density is observable, to determine whole of the SSC spectrum

Chapter 4.

Instrument

4.1 *Herschel*

Herschel space observatory (Pilbratt et al. 2010) launched on 14 May 2009 is the far to near infrared observation mission. the Spectral and Photometric Imaging REceiver (SPIRE; Griffin et al. 2010) and Photodetector Array Camera and Spectrometer (PACS; Poglitsch et al. 2010) onboard the *Herschel* performs the imagin observation. A combination of these two instruments operated in the photometer mode covers a wide FIR wavelength range of 70–500 μm, corresponding to the frequency range of $(0.6\text{–}4.3) \times 10^{12}$ Hz, where the hot spots are typically expected to exhibit the cooling break as mentioned above. Thanks to their reasonable photometrical sensitivity (typically $\gtrsim 10$ mJy) and moderate angular resolution (about 20 and 10 arcsec for SPIRE and PACS, respectively), these two instruments are applicable to the hot spots with a projected distance from its nucleus of larger than a few arcmin. *Chandra* (Weisskopf et al. 2000) performs the high resolution soft X-ray imaging and spectroscopy. The High Resolution Mirror Assembly of *Chandra* optics has a very sharp PSF size of 0.5 arcsec in FWHM, which is the best in current X-ray observatories. Therefore, the *Chandra* is able to investigate a detailed position and structure of the hot spot. The X-ray detecotrs of Advanced charge coupled device (CCD) Imaging Spectrometer (ACIS: Garmire et al. (2003)) covers the energy range of 0.3–10.0 keV.

4.2 *XMM-Newton*

XMM-Newton (Jansen et al. 2001) performs the high throughput imaging spectroscopy in a soft X-ray band. Three telescopes on the *XMM-Newtom* have a large effective area of 4,500 cm^2 at 1 keV, in total. Their field of view of size of 30×30 arcmin^2 and PSF size of ~ 5 arcsec in FWHM are well suited to the hot spot observation. Three X-ray CCD cameras (European Photon Imaging Camerras: EPICs) installed in the telescopes are two front-illuminated CCDs of Metal Oxcide Semi-conductors (MOS1,2 Turner et al. (2001)) and a back-illuminated pn type CCD (PN Strüder et al. (2001)). The EPICs cover the energy range of 0.2–10 keV.

4.3 *NuSTAR*

NuSTAR satellite (Harrison et al. 2013) realizes hard X-ray imaging spectroscopy. The equipped two co-aligned Walter-type I telescopes have almost the same field of view of the size of 13×13 arcmin^2, with an excellent Point Spread Function (PSF) of 18 arcsec in Full Width at Half Maximum (FWHM). The Pictor A western hot spot is 4 arcmin away from the nucleus. *NuSTAR* observes both the nucleus and the hot spot in a field of view and

clearly resolves them. The Focal Plane Module A and B (FPMA and B) covers the energy range of 3-79 keV with the pixelized CdZnTe detector arrays.

Chapter 5.

Hot spots of Cygnus A and Pictor A

5.1 Characters of Pic A and Cyg A among hot spots

5.2 Previous studies

5.2.1 Cygnus A

The hot spot named "D" of the FR-II radio galaxy Cygnus A, located at the end of its eastern jet (Bentley et al. 1975; Perley et al. 1984) is one of the best candidates for the FIR studies with *Herschel*. This hot spot has been extensively observed in radio, NIR and X-ray bands (Meisenheimer et al. 1989; Carilli et al. 1991; Wilson et al. 2000; Wright and Birkinshaw 2004; Stawarz et al. 2007). Its radio-to-X-ray spectrum is usually explained by the SSC process (Harris et al. 1994; Wilson et al. 2000; Stawarz et al. 2007). By artificially introducing a possible cooling break at the frequency of 0.5×10^{12} Hz into the SSC model, Stawarz et al. (2007) estimated the magnetic field strength of the hot spot as $B = 270$ μG for the radius of $R = 0.8$ kpc. The observed information of the hot spot D is utilised to investigate the properties of the jets, lobes and cocoons of this radio galaxy (e.g., Wilson et al. 2006; Yaji et al. 2010). Analytical and theoretical studies tried to evaluate the dynamics, energetics and plasma composition related to the jets, by connecting the physical quantities observed from the above components (e.g., Kino and Kawakatu 2005; Ito et al. 2008; Kino et al. 2012; Snios et al. 2018). However, as mentioned above, due to the FIR spectral gap in 10^{11}–10^{13} Hz, the cooling break has not yet been observationally confirmed, and there probably remain notable uncertainties in the physical parameters of the hot spot. From its relatively high radio flux density of ~ 10 Jy at 10 GHz and radio energy index of $\alpha \sim 1$, the FIR flux density of the hot spot is estimated as ~ 100 mJy at 10^{12} Hz, which is significantly high than the SPIRE and PACS sensitivities. Because of its large angular separation from the nucleus of Cygnus A as ~ 50 arcsec, the hot spot D is safely detectable by the two instruments without suffering from any nuclear contamination. Therefore, we investigate the FIR infrared spectrum of the hot spot to make sure of its cooling break, by utilising the *Herschel* SPIRE and PACS data.

5.2.2 Pictor A

The representative hot spot located at the western jet terminal of Pictor A is near us (the red shift of $z = 0.035$, Eracleous and Halpern (2004)) and has a large angular distance from the nucleus of 4 arcmin. In the good observational condition, some remarkable features are reported in multi-wavelength (Thomson et al. 1995; Wilson et al. 2001; Isobe et al. 2017, 2020; Thimmappa et al. 2020) and the hot spot is one of the most studied object. Tingay et al. (2008) discovered the sub parsec scale radio fine structure in the hot spot and suggested it to a

counterpart of the X-ray emission. Hardcastle et al. (2016) reported the possible month-scale X-ray flux decrease from the long-term *Chandra* observation and supported the fine structure scenario because of the compatibility between the time scale and the size of the fine structure. In addition to the decrease, they reported a possible spectral break around 2 keV. From the decrease and break, X-rays are considered to e emitted from the highest energy electrons. However there is some rooms for verification in these results due to the both/either the low statistics and/or narrow energy range. For example, there is no direct evidence of the cut-off feature corresponding to the maximum electron energy.

Chapter 6.

Observation and Analysis

6.1 FIR study of Cygnus A

6.1.1 FIR observation and analysis

Herschel Data

In order to investigate the FIR properties of the hot spot of Cygnus A, we utilised the FIR data obtained with the PACS and SPIRE photometers. The SPIRE photometer mapped Cygnus A on 2011 October 11 in the Large Map mode(Obs. ID of 1342230853), while the PACS photometers observed the object on 2011 December 24 with two pairs of cross-scan mappings in a scan speed of 20 arcsec s^{-1}. In the first cross-scan observation (Obs. ID of 1342235110 and 1342235111), the blue camera of the PACS photometer was operated at the wavelength of 70 μm, while in the second one (Obs. ID of 1342235112 and 1342235113) the 100 μm filter was adopted for the blue camera.

We retrieved the final release of the SPIRE and PACS science products from the Herschel Science Archive. We analysed the data with version 15.0.1 of the HERSCHEL INTERACTIVE PROCESSING ENVIRONMENT, by applying the corresponding SPIRE and PACS calibration trees, SPIRE_CAL_14_3 and PACS_CAL_77_0, respectively. We adopted the Level-2 science products for SPIRE imaging and photometry. For the PACS blue camera (i.e., 70 and 100 μm), we employed the Level-2.5 data, while we utilised the Level-3 products for the PACS red camera (160 μm). From the PACS image products, we analysed the HPPUNIMAP and HPPJSMAP maps, both of which are applicable to extended sources. We confirmed that the photometric results from the two maps were consistent with each other within 5 per cent. We, hereafter, adopt the HPPUNIMSP results because its photometric accuracy is slightly better at 70 μm.

FIR images

Figure 6.1 shows the 160 μm PACS (panel a) and 350 μm SPIRE (panel b) images around the radio galaxy Cygnus A on which the 5 GHz radio contours (Perley et al. 1984) are overlaid. The FIR emission from the nucleus of Cygnus A is significantly detected both in the PACS and SPIRE bands. The nucleus in the PACS image is truncated for clear visualization of fainter emission associated to the hot spots D. The inset inserted into panel (a) of Figure 6.1 shows the image around the nucleus with a different colour scale. The PACS image was registered to the radio one by referring to the nucleus position to correct the astrometric error ($\lesssim$ 1 arcsec for all the PACS bands). We ignored the astrometric error for all the SPIRE bands, because the typical astrometric uncertainty of *Herschel* (2 arcsec; Swinyard et al. 2010) is significantly smaller than the SPIRE pixel size (6–14 arcsec, dependent

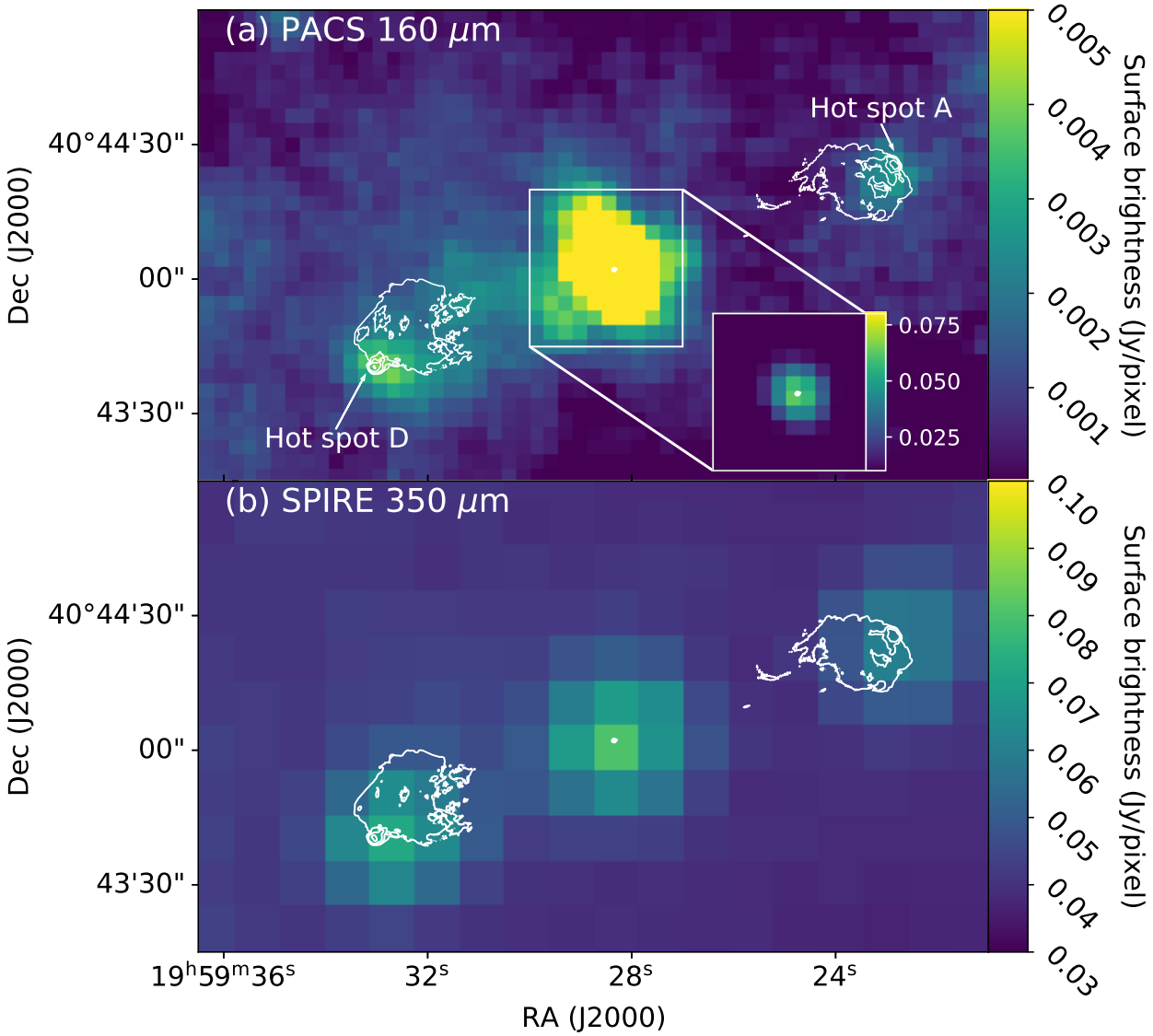

Figure6.1 Panel (a) shows the 160 μm PACS image of Cygnus A. Panel (b) shows the 350 μm SPIRE image. On both panels, the 5 GHz radio contours (Perley et al. 1984) are overlaid. The colour bar on the right of each panel shows the surface brightness in the unit of Jy pixel^{-1}. The arrows in panel (a) indicate the hot spot A and D. The inset in panel (a) indicates the PACS image with a different colour scale and VLA contours around the nuclei.

on the photometric band). The FIR sources associated with the radio hot spots A and D were cleary detected. In this paper, we focus on the FIR source corresponding to the hot spot D because the hot spot A is reported to be subjected to bright emission surrounding it in the NIR and optical bands (Stawarz et al. 2007).

Firstly, we investigated the spatial property of the FIR source using the PACS image, which has a better angular resolution than that of SPIRE. Figure 6.2 shows the 160 μm PACS close-up view around the hot spot D. The FIR source seems slightly extended in comparison to the PACS point spread function (PSF) with the size of $d_{\rm PSF}$=11.4 arcsec in the Full With at Half Maximum (FWHM) at 160 μm, shown with the white circle in Figure 6.2. The radio image reveals the fainter hot spot E to the $\sim$ 5 arcsec west of the hot spot D. Thus, in the PACS image, the FIR source is possibly contaminated by the hot spot E.

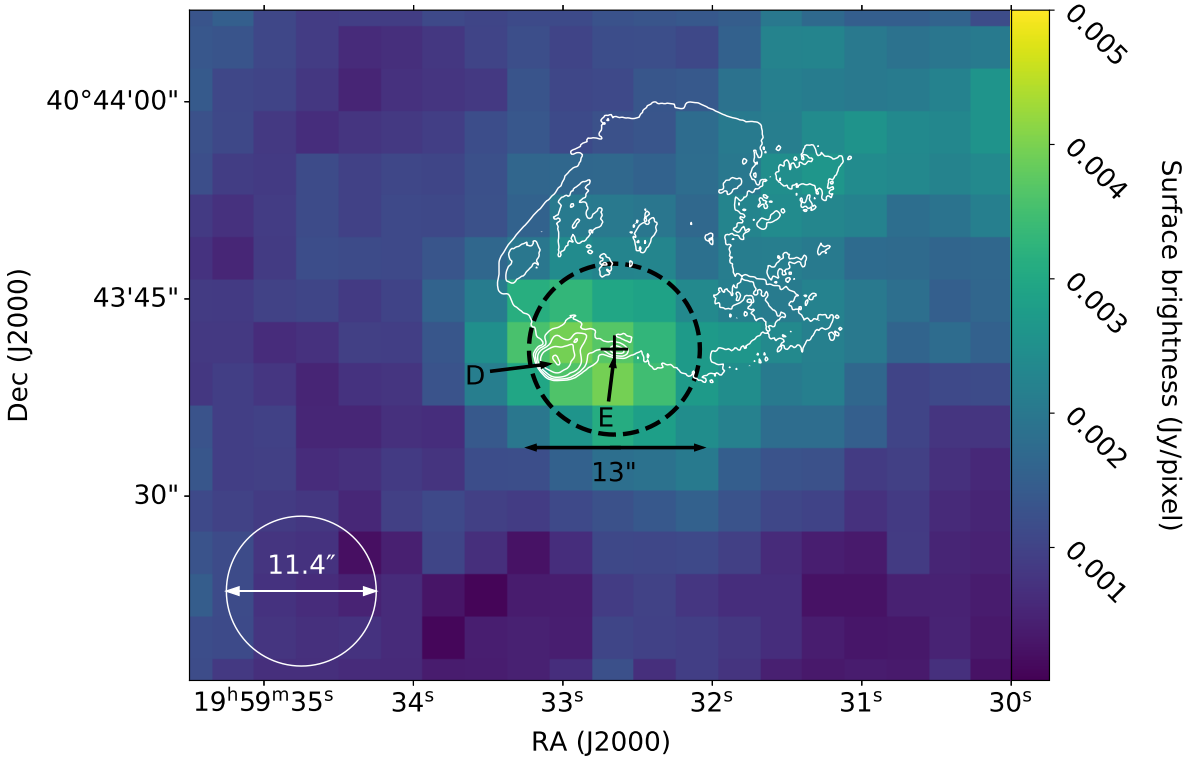

Figure6.2 The 160 μm image around the FIR source associated to the hot spot D observed by the PACS. The black dashed circle and the black cross indicate the apparent source size and position obtained by SUSSExtractor, respectively. The white solid circle shows the PSF size in the FWHM of PACS at 160 μm . The arrows labeled as D and E indicate the position of the radio hot spots D and E, respectively.

In order to evaluate the angular size of the FIR source, we applied SUSSEXtractor (Savage and Oliver 2007) to the PACS data by changing the apparent source size. No FIR source was found when the input source size was set to the PSF size. However, we detected the source for an input source size larger than the PSF size, except for a marginal detection at 70 μm. We adopted the apparent FWHM source size ($d_{\rm ap}$) which gives the largest signal to noise (SN) ratio. Table 6.1 summarises the PACS result of the source detection. In the 160 μm image, we measured the apparent source size as $d_{\rm ap}$ = 13 arcsec which is larger than the PSF size of $d_{\rm PSF}$ = 11.4 arcsec.

The FIR source position determined by SUSSEXtractor is significantly shifted from the radio hot spot D, and the angular offset of ($\Delta\theta_{\rm RA}$, $\Delta\theta_{\rm Dec}$) = (-4.3 ± 1.1, 0.8 ± 1.1) arcsec at 160 μm is not negligible in comparison with the PSF size. In Figure 6.2, we show the FIR source position determined with SUSSEXtractor and apparent source size with the black cross and dashed black circle, respectively. Although the hot spot D is on the brightest pixel of the PACS image, the source is shifted toward the radio hot spot E. Besides, the apparent source size encompasses both the hot spots D and E. These imply the FIR emission mainly originates in the hot spot D with a notable contamination from the hot spot E. We calculated the deconvoluted source size as $d_{\rm src} = \sqrt{d_{\rm ap}^2 - d_{\rm PSF}^2}$. The derived source size in the PACS images is summarised in Table 6.1. The deconvolved source size ($d_{\rm src}$ = 6.2 arcsec at 160 μm) is roughly consistent with the angular separation between the hot spots D and E. This result also

Table6.1 Summary of the FIR source spatial property

instrument	λ [a] (μm)	$d_{\rm PSF}$ [b] arcsec	$\Delta\theta_{\rm RA}$ [c] arcsec	$\Delta\theta_{\rm Dec}$ [c] arcsec	$d_{\rm src}$ [d] FWHM (arcsec)	SN ratio
SPIRE	500	35	-1.5 $\pm$ 0.4	3.5 $\pm$ 0.4	point like	56
	350	24	-1.3 $\pm$ 0.3	1.6 $\pm$ 0.3	point like	70
	250	18	-2.7 $\pm$ 0.4	1.0 $\pm$ 0.4	point like	29
PACS	160	11.4	-4.3 $\pm$ 1.1	0.8 $\pm$ 1.1	6.2	7.4
	100	6.8	-2.5 $\pm$ 1.1	0.2 $\pm$ 1.1	9.6	6.7
	70	5.6	-2.5 $\pm$ 1.2	0.4 $\pm$ 1.2	6.5	4.5

aThe effective wavelength

b The averaged PSF size (FWHM), taken from the calibration tree

c The angular offsets of the FIR source from the brightness centre of the hot spot D in 5 GHz.

d The source size (FWHM) calculated by deconvolving the PSF from the apparent source size.

implies the contamination from the hot spot E.

The FIR source seems point-like in the SPIRE image displayed in panel (a) of Figure 6.1. The point-like nature of the FIR source in the SPIRE band seems reasonable, since the deconvolved source size with the PACS (i.e., 6.2 arcsec at 160 μm) is smaller than the SPIRE PSF (see Table 6.1). Thus, we performed SUSSEXtractor by adopting the SPIRE PSF size. We significantly detected the source with an SN ratio is 70 in the 350 μm image. Table 6.1 also summarises the result of the SPIRE source detection. The derived angular offset of ($\Delta\theta_{\rm RA}$, $\Delta\theta_{\rm Dec}$) = (-1.3 ± 0.3, 1.6 ± 0.3) arcsec at 250 μm is negligible in comparison with the PSF size of $d_{\rm PSF}$ = 24 arcsec even at 250 μm, where the spatial resolution is highest among the SPIRE phtometric bands. Thus, we did not resolve the hot spots D and E due to the SPIRE angular resolution.

6.1.2 FIR photometry

We measure the PACS and SPIRE flux of the FIR source associated with the hot spot D. Since the hot spot E is not fully resolved with the PACS and SPIRE, as shown in section 6.1.1, we here evaluate the sum flux of the hot spots D and E by adopting aperture photometry. We decompose the source flux into those of D and E by utilising the multi-wavelength spectra in section 6.1.3.

The source and background apertures we adopted for the PACS photometry at 160 μm is shown in panel (a) of Figure 6.3, while those for the SPIRE photometry at 350 μm is indicated in panel (b). The radius of the source aperture for the individual SPIRE and PACS photometric bands is summarised in Table 6.2. For the SPIRE photometry, the FIR source position obtained from SUSSEXtractor is employed as the centre of the source aperture. The radius of the source aperture is determined to avoid contamination from the nucleus. To evaluated the spatial fluctuation of the background flux density, the six background apertures are selected from the region around the FIR source. We did not put any background aperture between the FIR source and nucleus to avoid contamination from the nucleus and possibly from the lobe. For the background regions, we adopted the same aperture radius as for the source one. At the 500 μm SPIRE band, we did not evaluate the FIR source flux, because the nuclear contamination is expected to be severe due to the poor angular resolution. For the PACS photometry, the radio position of the hot spot D is employed as the source position, instead of that determined with SUSSEXtractor

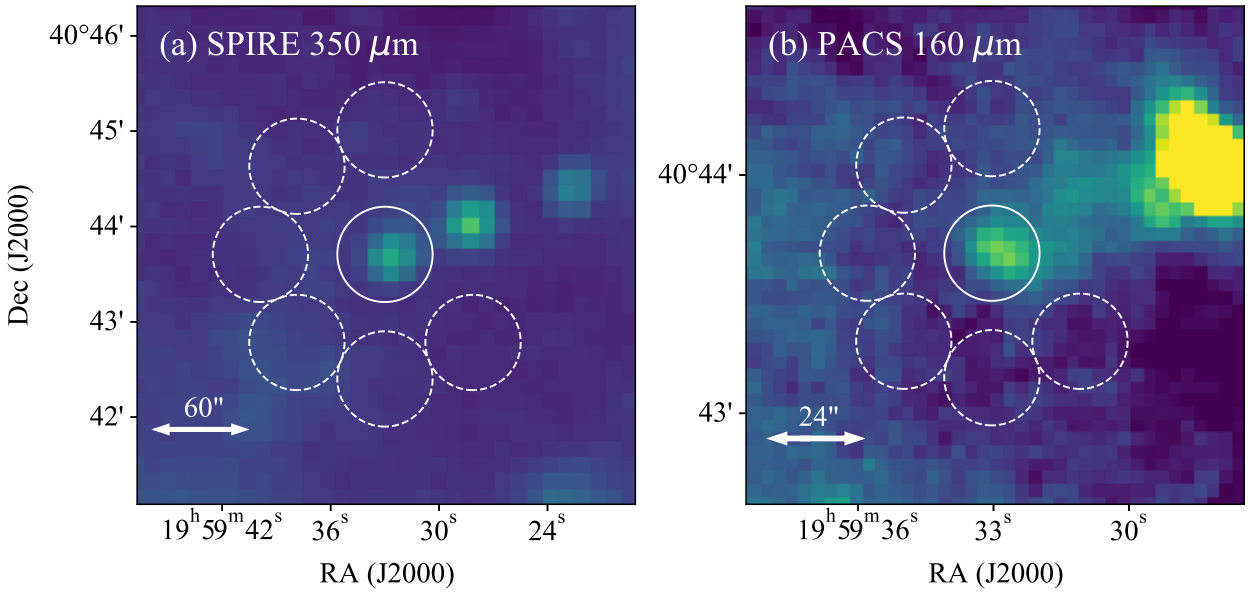

Figure6.3 The source region and background regions used for the photomery with SPIRE (panel a) and PACS (panel b). The white solid circle and dashed circles indicate the source and background regions, respectively.

because it nearly coincides with the brightness peak of the FIR source on the PACS image. The source aperture size is determined to safely include the emission from the hot spots D and E but excludes the nuclear contamination and diffuse emission possibly associated with the lobe. Similar to the SPIRE photometry, the same radius as for the source region is adopted for the background regions.

We performed the SPIRE and PACS photometry by using the individual background regions. Following the standard manner, we adopted the standard deviation of the fluxes of the six background regions as the photometric error. The aperture correction was performed to the measured flux densities by retrieving the correction factor for the adopted source radius from the calibration tree. We adopted the power-law (PL) spectrum with an energy index of α = 1 for the colour correction. At least in the range of α = 1–2, the colour correction has only a minor contribution with a correction factor of < 1 and < 0.1 per cent for SPIRE and PACS, respectively. In Table 6.2, we summarise the aperture-and-colour corrected flux density (F_ν) of the FIR source in Table 2, together with the adopted correction factor ($C_{\rm cor}$). The corrected flux densities are derived as F_ν =199±58 and 92.3±13 mJy in the SPIRE 350 and the PACS 160 μm photometric bands, respectively.

We show the obtained FIR spectrum of the source in Figure 6.4. The FIR spectrum is successfully reproduced by the PL model (χ^2/d.o.f. = 3.55/3), as shown with the dashed line in Figure 6.4. The energy index of $\alpha = 1.64 \pm 0.17$ and the flux density at 10^{12} Hz of 0.26 ± 0.04 Jy are obtained. Although the measured energy index is higher than that adopted for the colour correction (α = 1), the difference in the correction factor between these indices is negligible.

6.1.3 Spectrum of the hot spot D

Subtraction of the contamination from the hot spot E

In order to investigate the spectral property of the FIR source, we compare its FIR Spectral Energy Distribution (SED) with the radio and NIR data of the hot spot D and E, taken from Lazio et al. (2006), Carilli et al. (1991),

Table6.2 Summary of the SPIRE and PACS photometry

instrument	λ	ν [a]	aperture radius	$C_{\rm cor}$ [b]	$F_{\rm cor}$ [c]
	μm	10^{11}Hz	arcsec		mJy
SPIRE	350	8.6	30	1.240	291 ± 66
	250	12	22	1.283	199 ± 58
PACS	160	19	12	1.49	92.3 ± 13
	100	30	12	1.29	50.7 ± 9.4
	70	43	12	1.25	12.6 ± 7.5

a The frequency corresponding to the effective wavelength of λ

b The correction factor including the colour and aperture correction

c The aperture and colour corrected flux density of the FIR source

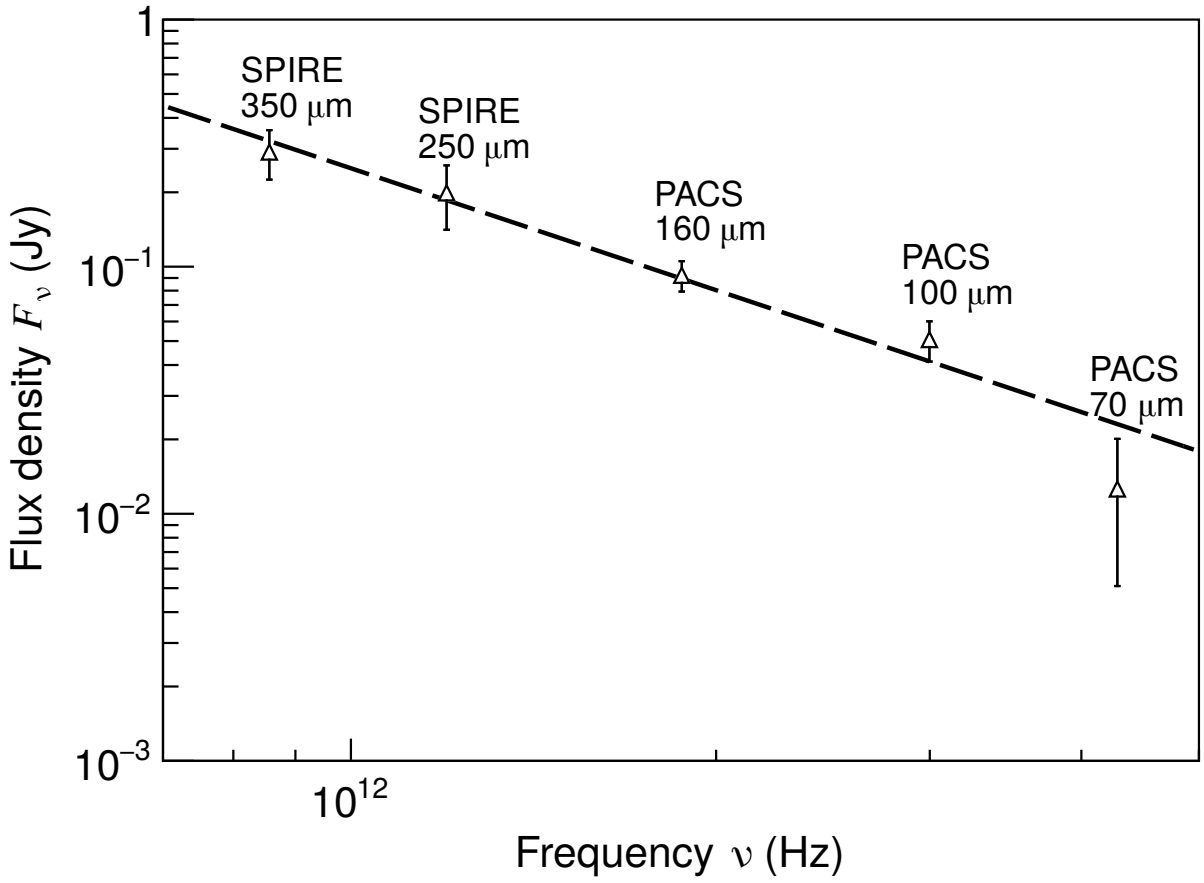

Figure6.4 The FIR spectrum of the source associated with the hot spot D obtained in the PACS and SPIRE phtometry. The open triangles show the flux density of the source, while the dashed line presents the best-fit PL model.

Table6.3 Estimated Flux densities of hot spot D and E.

instrument	λ	ν	$F_{\rm E,fit}{}^a$	$F_{\rm D}{}^b$
	μm	10^{11} Hz	mJy	mJy
SPIRE	350	8.6	22.0 ± 2.9	269 ± 66
	250	12	15.4 ± 2.2	185 ± 58
PACS	160	19	9.4 ± 1.5	83 ± 13
	100	40	5.3 ± 1.0	45.4 ± 9.4
	70	43	3.4 ± 0.7	9.2 ± 7.5

a The FIR flux density of the hot spot E calculated from the best-fit CPL model.

b The FIR flux density of the hot spot D calculated as $F_{\rm D} = F_{\rm cor} - F_{\rm E,fit}$

Wright and Birkinshaw (2004) and Stawarz et al. (2007). We show the radio to NIR SED of the hot spots D and E in Figure 6.5. In the radio band, both hot spots D and E exhibit a flat SED with an energy index of $\alpha \sim 1$, while of hot spot D is brighter than that of the hot spot E by an order of magnitude. Except for the 70 μm, the obtained FIR flux is slightly higher than a simple PL extrapolation of the radio flux from the hot spot D. These results suggests that the FIR flux of the source is dominated by the emission from the hot spot D with a possible contamination from the hot spot E.

To subtract the contamination from the hot spot E, we estimate the FIR spectrum of the hot spot E by interpolating the radio and NIR spectrum. The hot spot E has a lower NIR flux than the simple PL extrapolation of the radio spectrum. Thus, we fitted the radio to NIR spectrum of the hot spot E with the cut-off power law (CPL) model described as $F_\nu \propto \nu^{-\alpha} \exp\left(-\nu/\nu_{\rm c}\right)$, where ν_c denotes the cut-off frequency. The dashed line in Figure 6.5 shows the best-fit CPL model ($\chi^2/{\rm d.o.f.} = 6/3$), with the flux density at 10 GHz of F_ν(10 GHz) = 1.8 ± 0.1 Jy, the energy index of α = 0.97 ± 0.04, and the cut-off frequency of ν_c = $(1.1 \pm 0.4) \times 10^{13}$ Hz. The evaluated FIR flux density of the hot spot E ($F_{\nu,{\rm E-fit}}$) is about 10 per cent of the FIR flux density obtained from the aperture photometry (i.e. $F_{\nu,{\rm E-fit}}/F_\nu \sim 0.1$), except for at 70 μm with $F_{\nu,{\rm E-fit}}/F_\nu$ = 0.3. By subtracting the flux of the hot spot E from the measured FIR flux (F_ν), we estimated the FIR flux of the hot spot D (i.e., $F_{\nu,{\rm D}} = F_\nu - F_{\nu,{\rm E-fit}}$). We summarise $F_{\nu,{\rm D}}$ and $F_{\nu,{\rm E,fit}}$ in Table 6.3. At the 160 μm PACS band, the FIR fluxes of the hot spots D and E are evaluated as $F_{\nu,{\rm D}}$ = 83±13 mJy and $F_{\nu,{\rm E-fit}}$ = 9.4±1.5 mJy. As a result of the subtraction of the contamination from the hot spot E, the derived FIR spectrum of the hot spot D seems to smoothly connect to the radio spectrum within the errors, except for the 70 μm band (see Figure 6.6).

Spectral modelling of the hot spot D

We investigate the spectral properties of the hot spot D. Figure 6.6 clearly shows that a simple PL does not reproduce the radio to NIR spectrum. Therefore, we first tried a CPL model to the observed spectrum, and derived the parameters as listed in Table 6.4. Although the CPL model, indicated with the dashed line in panel (a) of Figure 6.6, is statistically acceptable (χ^2/d.o.f. = 6.78/8), we noticed several discrepancies between the observed and model spectra. The best-fit CPL mode seems slightly flatter than the observed FIR spectrum of the hot spot D, and hence, it possibly overestimates the 70 μm flux. This result suggests a spectral break in the FIR band.

In order to evaluate the possible break, we next adopted a broken PL model, subjected to a high energy cut-off

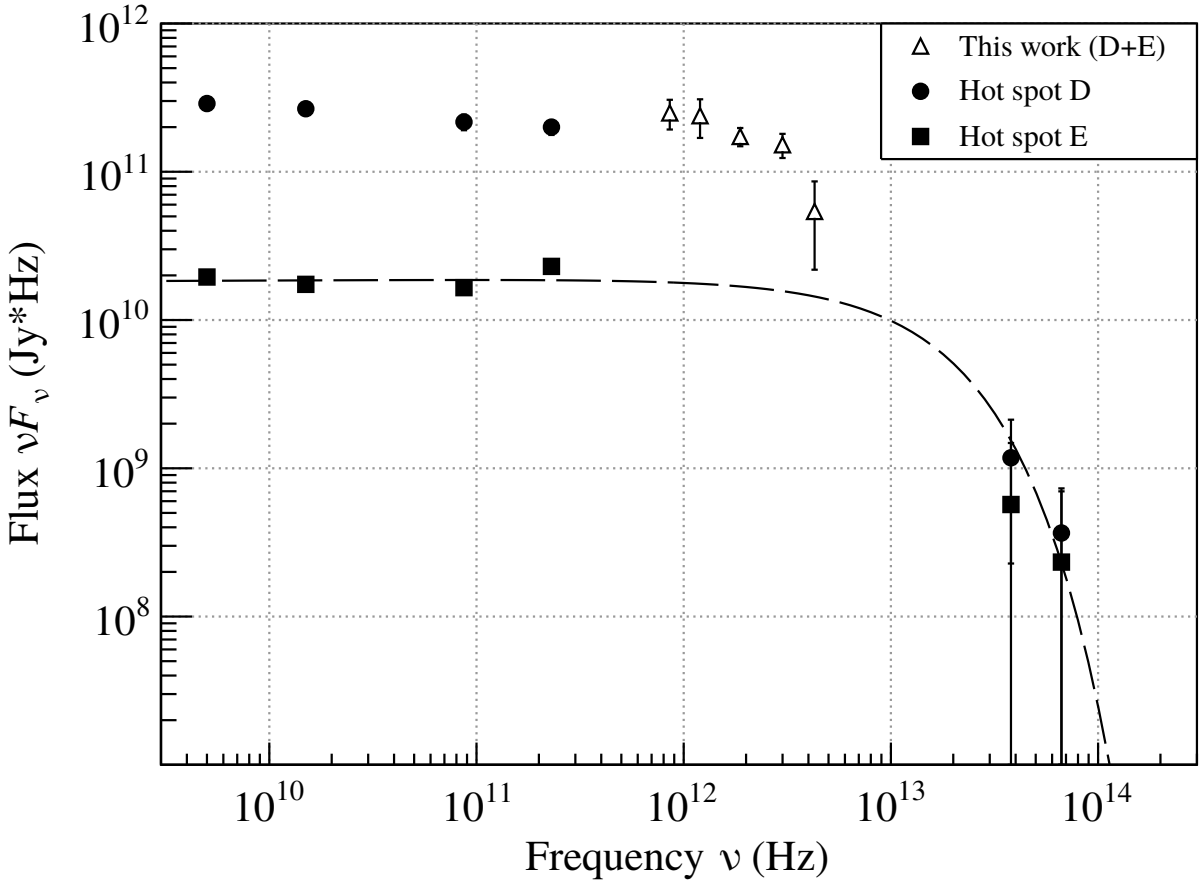

Figure6.5 Broadband SED of the hot spot D and E. The open trangles show the SED of the FIR source associated with the hot spot D obtained in this work. The filled circles and filled squares plots the spectrum of the hot spot D and E (Lazio et al. 2006; Carilli et al. 1991; Wright and Birkinshaw 2004; Stawarz et al. 2007), respectively. The dashed line displays the best-fit CPL model to the spectrum of the hot spot E.

written as

$$F_{\nu,\mathrm{D}} \propto \begin{cases} \nu^{-\alpha} \exp(-\nu/\nu_{\mathrm{c}}) & \text{for } \nu < \nu_{\mathrm{br}} \\ \nu^{-(\alpha+\Delta\alpha)} \exp(-\nu/\nu_{\mathrm{c}}) & \text{for } \nu > \nu_{\mathrm{br}} \end{cases} \tag{6.1}$$

Hereafter, we simply refer to the model as the Broken PL (BPL) model. We fitted the spectrum with the BPL model and found that the model improved the fitting. However, due to the degeneracy between the change of the energy index ($\Delta\alpha$) and the break frequency (ν_{br}), it is difficult to determine the parameters simultaneously. Thus, we searched for the range of $\Delta\alpha$ in which the fit is significantly improved. As a result, we found that in the range of $0.23 < \Delta\alpha < 7$, the model reduces the chi-square by at least 1 in comparison to the CPL model. Therefore, we fixed the index change at $\Delta\alpha = 0.5$ to constrain the break frequency, since it is theoretically consistent with the index change predicted from the diffusive shock acceleration under the continuous energy injection, accompanied with a radiative cooling (Heavens and Meisenheimer 1987; Carilli et al. 1991). Stawarz et al. (2007) interpreted the spectrum of the hot spot D, without the FIR data, by the BPL model with $\Delta\alpha = 0.5$, and derived the parameters denoted as "BPL (Stawarz)" in Table 6.4. Although the BPL model with the parameters by Stawarz et al. (2007) agrees with the radio data, it significantly underestimates the FIR spectrum, as shown with the dash-dotted line in panel (a) of Figure 6.6. This suggests that the break frequency is higher than their result ($\nu_{\mathrm{br}} = 0.5 \times 10^{12}$ Hz;

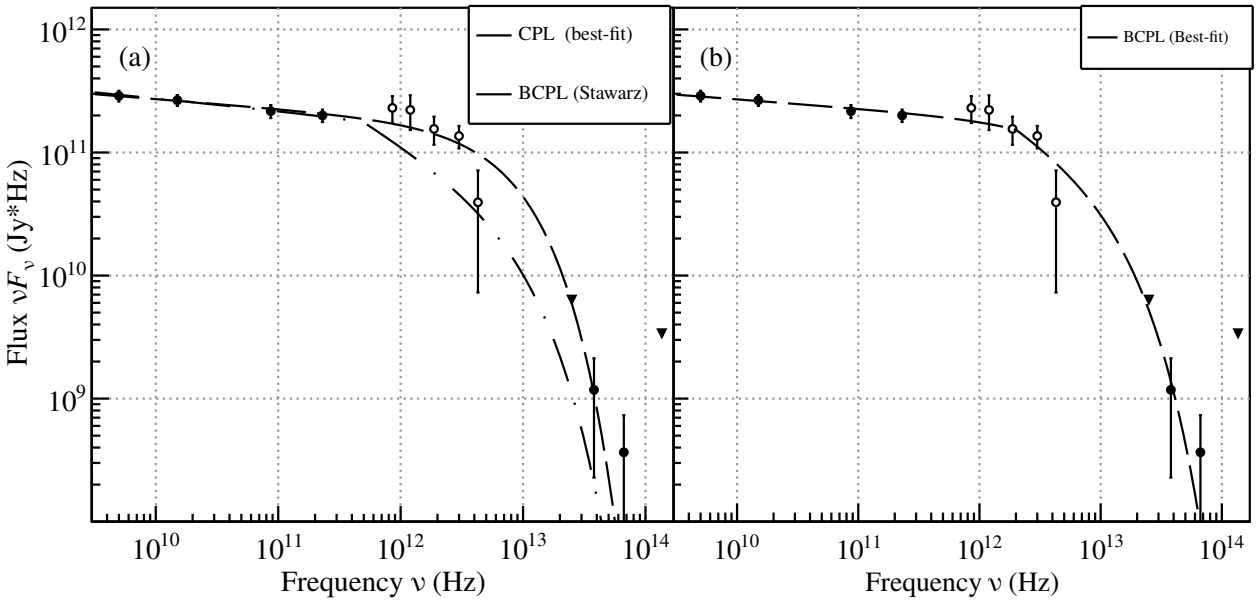

Figure6.6 SED of the hot spot D. The open circles show the FIR spectrum of hot spot D, $F_{\rm D}$, after subtracting the contamination from the hot spot E. The filled circles show the radio and NIR spectrum of the hot spot D form literature. The dashed and dash-dotted line in panel (a) show the best-fit CPL model and the CBPL model in (Stawarz et al. 2007) , respectively. The dashed line in panel (b) shows the best-fit BCPL model.

Table6.4 Best-fit parameters to the spectra of the hot spot D.

model	$F_{\rm 10GHz}{}^{a}$ Jy	α^{b}	$\nu_{\rm br}{}^{c}$ Hz	$\nu_{\rm c}{}^{d}$ Hz	χ^2/d.o.f.
CPL	27±1.7	1.06±0.03	—	$(0.8\pm0.1)\times10^{13}$	6.7/8
CBPL (Stawarz)	27	1.1	0.5×10^{12}	0.9×10^{13}	20/11
CBPL	27±1.8	1.07±0.03	$2.0^{+1.2}_{-0.8}\times10^{12}$	$(1.2\pm0.3)\times10^{13}$	4.8/7

a The flux density at 10 GHz

b The energy index at lower frequency than the break and cut-off

c The break frequency of the CBPL model

d The cut-off frequency

Stawarz et al. 2007).

To determine precisely the break frequency, we re-fitted the BPL model to the spectrum of the hot spot D, by including the FIR data. The dashed line in panel (b) in Figure 6.6 shows the best-fit BPL model (χ^2/d.o.f. = 4.8/7), which successfully reproduces the overall spectrum in the radio, FIR and NIR ranges. The best-fit parameters are summarised in Table 6.4. By adopting the BPL model, the fit is slightly improved compared to the CPL model; the null-hypothesis probability of the F-test between the best-fit CPL and BPL is 14 per cent. The best-fit break frequency is determined as $\nu_{\rm br} = 2.0^{+1.2}_{-0.8} \times 10^{12}$ Hz. The derived break frequency is significantly higher than that adopted in Stawarz et al. (2007). The other parameters are found to stay almost unchanged from those of the CPL model and those of the BPL model in Stawarz et al. (2007). Thanks to the FIR data, we have succeeded in determining the break frequency of the hot spot D for the first time.

Table6.5 Observation IDs and dates of the *Chandra* observations

Obs. ID	date	Epoch	Obs. ID	date	Epoch
346	2000-01-18	1	14221	2012-11-06	5
3090	2002-09-17	2	15580	2012-11-08	5
4369	2002-09-22	2	15593	2013-08-23	6
12039	2009-12-07	3	14222	2014-01-17	7
12040	2009-12-09	3	14223	2014-04-21	8
11586	2009-12-12	3	16478	2015-01-09	9
14357	2012-06-17	4	17574	2015-01-10	9

6.2 UV to hard X-ray study of Pictor A

6.2.1 *Chandra*

Chandra observed Pictor A region 14 times between 2000 and 2015. The obsevation IDs and the dates are tabulated in Table 6.5. These observation results are reported in by papers. The X-ray hot spot was found to be well associated to the radio one and identified by the *Chandra* (Wilson et al. 2001; Thimmappa et al. 2020). Furthermore, Hardcastle et al. (2016) investigated all observations and reported an X-ray flux decrease of the hot spot.

We re-analyzed the data of the observations to confirm the X-ray emission from the hot spot and re-evaluate the time variability. In the following analysis procedures, we used the latest softwares (`ciao-4.13`, Fruscione et al. (2006)) and the calibration database (`CALDB 4.9.5`) at our analysis phase, which are newer than those used in the literature. We performed the data reduction using `chandra_repro` script. The exposure times after the reduction are almost the same as those in the literature, a total of which is 460 ksec.

6.2.2 *XMM-Newton*

XMM-Newton observed the Pictor A region on 2001 March 17 and on 2005 January 14. The observation IDs are 0090050801 and 0206039010, respectively. Utilizing the data, Grandi et al. (2003) and Migliori et al. (2007) studied the eastern and the western lobes of Pictor A.

In the following analysis, we employed only the MOS1 and PN data obtained in the second observation. In the first observation, the MOS cameras were operated in the small window mode, and failed to observe the western hot spot. The PN observed the hot spot but it is located near the detector gap. In the second occasion, on the other hand, the hot spot was successfully observed by both MOS1 and PN, but was out of the field of view of MOS2 as it was operated in the small window mode. Therefore we analyzed the MOS1 and PN data obtained in the second occasion. We performed the data reduction using the Science Analysis Software (SAS) version 19.0.0. The effective exposure times are 49 and 30 ksec for MOS1 and PN, respectively.

We surveyed the OM source catalog of Serendipitous Ultraviolet Source Survey catalog of `OM SUSS 4.1` (Page et al. 2012) and found out the OM counterpart named "XMMOM J051926.2-454554" which locates within 1" of the western hotspot. Table 6.6 summarized the counterpart of flux density and detection significance in each filter. The counterpart was significantly detected in the exposures with five different wavelength filters.

Table6.6 Summary of ON counterpart

Filter	effective wavelength	Flux density	significance
B	450	1.10 ± 0.04	35.2
U	344	1.26 ± 0.04	36.7
UVW1	291	1.62 ± 0.07	26.9
UVM2	231	1.44 ± 0.14	10.9
UVW2	212	1.72 ± 0.32	5.5

6.2.3 *NuSTAR*

In this work, we utilized the archival data aiming at the Pictor A nucleus (obs.ID 60101047002). The observation was conducted between December 3 and 6 in 2015. For the *NuSTAR* data reduction and analysis, we used the software of NUSTARDAS ver. 2.0.0 and calibration database of CALDB ver 20210524. We performed the data reduction using `nupipeline` script with a standard criteria for science observation named "SCIENCE". The resultant effective exposure is 109 ksec.

6.2.4 Image analysis

Before analyzing the *NuSTAR* and *XMM-Newton* images which are firstly performed on the hot spot in this paper, we reviewed the spatial property of the hot spot on the *Chandra* image. We employed the observation of Obs.ID 4369, in which observation the obtained X-ray image located at the center of the field of view coincides with the radio hot spot. The X-ray hot spot is resolved, and the it extended roughly 1 arcsec in FWHM, consistent with the result in Thimmappa et al. (2020).

XMM-Newton image

We then analized the images of *XMM-Newton*/MOS1 and PN. We confirmed the point-like sources associated with the hot spot as mentioned in Grandi et al. (2003) and Migliori et al. (2007). We see the spatial offsets from the source to the hot spot by 1.3 and 2.2 arcsec in MOS1 and PN images, respectively. These are consistent within 2σ-level pointing accuracy of 3.0 and 2.0 arcsec in MOS1 and PN, respectively (Kirsch et al. 2004). Considering the PSF sizes of 5 and 6 arcsec for MOS1 and PN, respectively, the source size is consistent with the hot spot size determined by the *Chandra*. In addition, there is no confusing source in *Chandra* image. Therefore, we considered the source in *XMM-Newton* images as the hot spot.

NuSTAR image

We checked both FPMA and FPMB exposure-corrected images and found two sources as shown in panel (a) of Figure 6.7. The exposure map is generated by the `nuexpomap` script. The image is smoothed by Gaussian with a standard deviation of 4.8 arcsec, corresponding to twice of pixel size. The brighter source at the center of the image is Pictor A nucleus, of which detailed spectral analysis was already reported in Kang et al. (2020). In addition to the nucleus, we see a source in the north west. The enlarged image is shown in panel (b) of Figure 6.7, with overlaid contours of *Chandra* image. The source is associated with the hot spot.

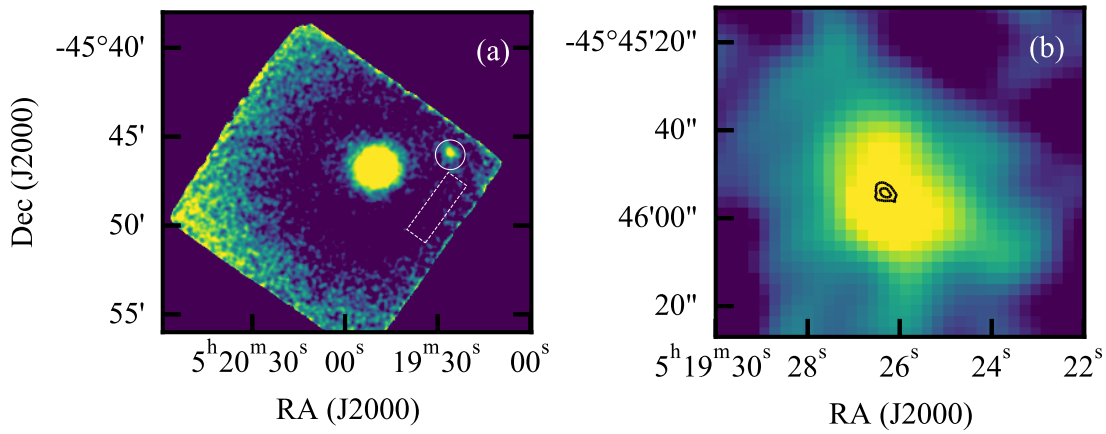

Figure6.7 (a)FPMA image smoothed with a Gaussian whose size is corresponding to a PSF size of 50 arcsec (HPD), using events in 85-460 PHA channels roughly corresponding to 3-20 keV. (b) The enlarged image around the western region overlaid the contour of *Chandra* image.

To investigate the candidate hard X-ray emission of the hot spot, we evaluated the spatial properties quantitatively. We compared a center of the brightest pixel as the position of the candidate to the hot spot position determined in *Chandra* image. There are consistent in 2.5 and 2.8 arcsec in FPAM, and FPMB images, respectively. These are smaller than the pointing uncertainty of the *NuSTAR* of $\gtrsim$ 5.5 arcsec (Harp et al. 2010) and consistent with the position of the hot spot.

The apparent size is measured on the smoothed image as 27 ± 2.4 arcsec in FWHM. The size is consistent with the apparent size of the nucleus. Since the hot spot size is negligible in comparison with the PSF, the obtained image size is consistent with the hot spot.

In addition, there is no other bright X-ray source around the hot spot as mentioned above. Therefore, we safely concluded that the observed source is a hard X-ray counterpart of the hot spot. This is the first detection of the jet termination hot spots with *NuSTAR*.

6.2.5 Time variability analysis using *Chandra* data

Hardcastle et al. (2016) reported an interesting X-ray behavior of the hot spot – a month-scale flux decrease of the hot spot. They pointed out that it could be caused by energy losses of the highest energy electrons. However, the flux decrease is accompanied by a spectral hardening, which imply a flux decrease in the low-energy band (see, Hardcastle et al. (2016); Thimmappa et al. (2020)). Below 1 keV, we carefully examine unexpected increase of molecular contamination on the detector surface which reduces the effective area. In fact, a position dependence of the contamination is reported, although the time variation at the typical aim point is calibrated and corrected with the CALDB file (Plucinsky et al. 2018).

We investigated the time variation of the count rate of the hot spot. We measured count rates in low-energy (0.3–1.0 keV), which is sensitive to contamination, and high-energy (1.0–7.0 keV) bands for comparison, sepalately.

Here, we divided the observation data into 9 epochs, according to Hardcastle et al. (2016). Figure 6.8 shows the count rates as a function of time. In the low energy band, the count rates in epochs 4,6,8, and 9 are about 20 per cent lower than those in the other epochs, while there is no significant fluctuation in the high energy band.

Figure 6.9 shows the source position on the detectors for each epoch. In epochs 4, 6, and 8, the hot spot is close to the chip gap or observed by a different ACIS chip. In these cases, we cannot ignore the systematic uncertainties. To examine the apparent decrease in epoch 9, we also investigated the count rate variation for a calibration source, the supernova remnant E0102, during this period. E0102 has been observed at three different locations on the detector, indicated as low-Y, mid-Y, and high-Y in Figure 6.9. The obtained count rates and the locations are also shown in Figures 6.8 and 6.9, respectively. We see the count rates on high- and low-Y positions have decreased since 2015. This trend indicates the contamination effect causes the apparent decrease of the count rates on low- and high-Y positions. The hot spot position in epoch 9 is near the high-Y location. Thus, we regard the apparent decrease in epoch 9 was caused by artifacts. By considering the complex contamination effect, we see no evidence of the variation during the observation epochs. For more detailed investigations on the time variability, it is important to carefully evaluate the contamination build-up. The results from X-ray all sky survey performed by *eROSITA* (Predehl et al. 2021) will provide us with an excellent opportunity for this purpose.

6.2.6 X-ray Spectral analysis

XMM-Newton spectrum

Here we investigated the spectrum obtained from *XMM-Newton*'s second observation of Pictor A. We carried out a circular region of 18 arcsec in radius centered at the centroid of the hot spot for the source. To determine the background region, we searched for the point source via `edetect_chain` script. Then, we extracted a background spectrum from a circular region with a radius of 36 arcsec excluding any detected source. We adopted the same procedure of the spectral extraction for MOS1 and PN. The source emission dominates the background one in the energy range of 0.2–10.0 keV in both of the MOS1 and PN. The spectral analysis hereafter were performed with `XSPEC` (Arnaud 1996) version 12.11.1 in `HEAsoft` package version 6.28.

We fitted the background-subtracted spectrum with an absorbed power-law model, described as `tbabs*pegpwrlw` in `XSPEC`, using χ^2 statistics. In the fitting, we fixed the hydrogen column density to the Galactic value of $N_{\rm H}$=3.6$\times$10^{20} atoms cm^{-2} obtained from HI4PI[*1] (HI4PI Collaboration et al. 2016). The solar abundance table used in `XSPEC` is obtaned from Anders and Grevesse (1989). Figure 6.10 shows the spectra and the best-fit models, and the best-fit parameters and fitting range are summarized in Table 6.7. The models well reproduce the spectra with χ^2/d.o.f. = 97/90 and 197/181 for MOS1 and PN, respectively.

To check the consistency between the MOS1 and PN spectra, we compared the confidence contours. As shown in Figure 6.11, the contours are consistent with each other at 68% confidence level. Then, we fitted the MOS1 and PN spectra simultaneously. The best-fit parameters and the confidence contours are shown in Figure 6.11 and Table 6.7, respectively. There is no significant difference between the joint and individual fittings.

Chandra Spectrum

We analyzed the combined *Chandra* spectrum. To avoid the possible contamination effect, we used the spectrum above 1.5 keV. We adopted the circular region with a radius of 8 arcsec and the annulus region with the inner

[*1] The $N_{\rm H}$ value can be calculated in the website at https://heasarc.gsfc.nasa.gov/cgi-bin/Tools/w3nh/w3nh.pl

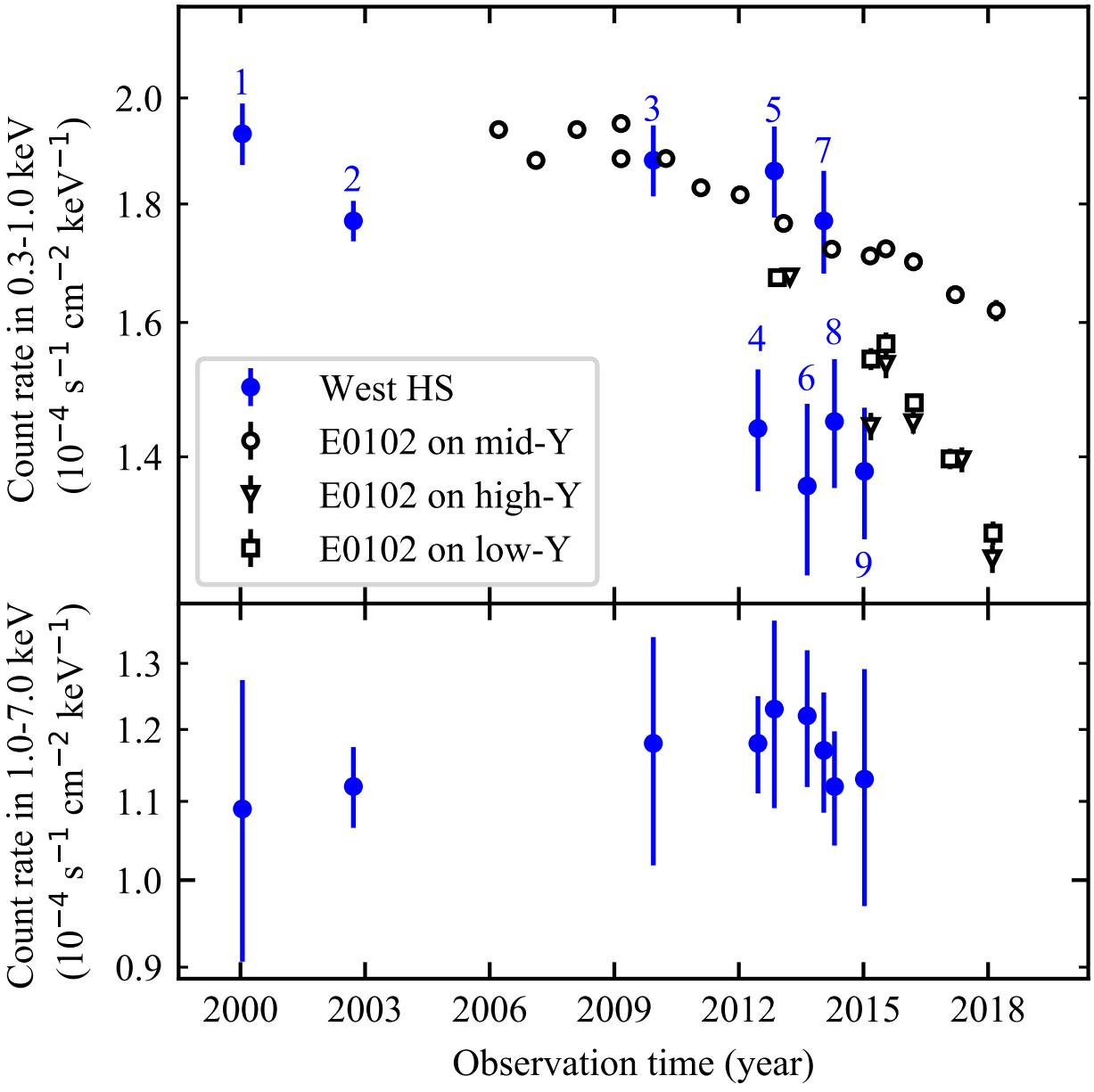

Figure6.8 The effective area corrected count rate of the hot spot and E0102 are shown. The blue filled circles indicate the count rates of hot spot and accompanying numbers indicates a corresponding epoch. The open circles, open triangles and open squares are indicates the E0102 at the mid, high and low-Y positions. The upper panel is the low energy band of 0.3-1.0 keV. The lower panel is the high energy band of 1.0-7.0 keV.

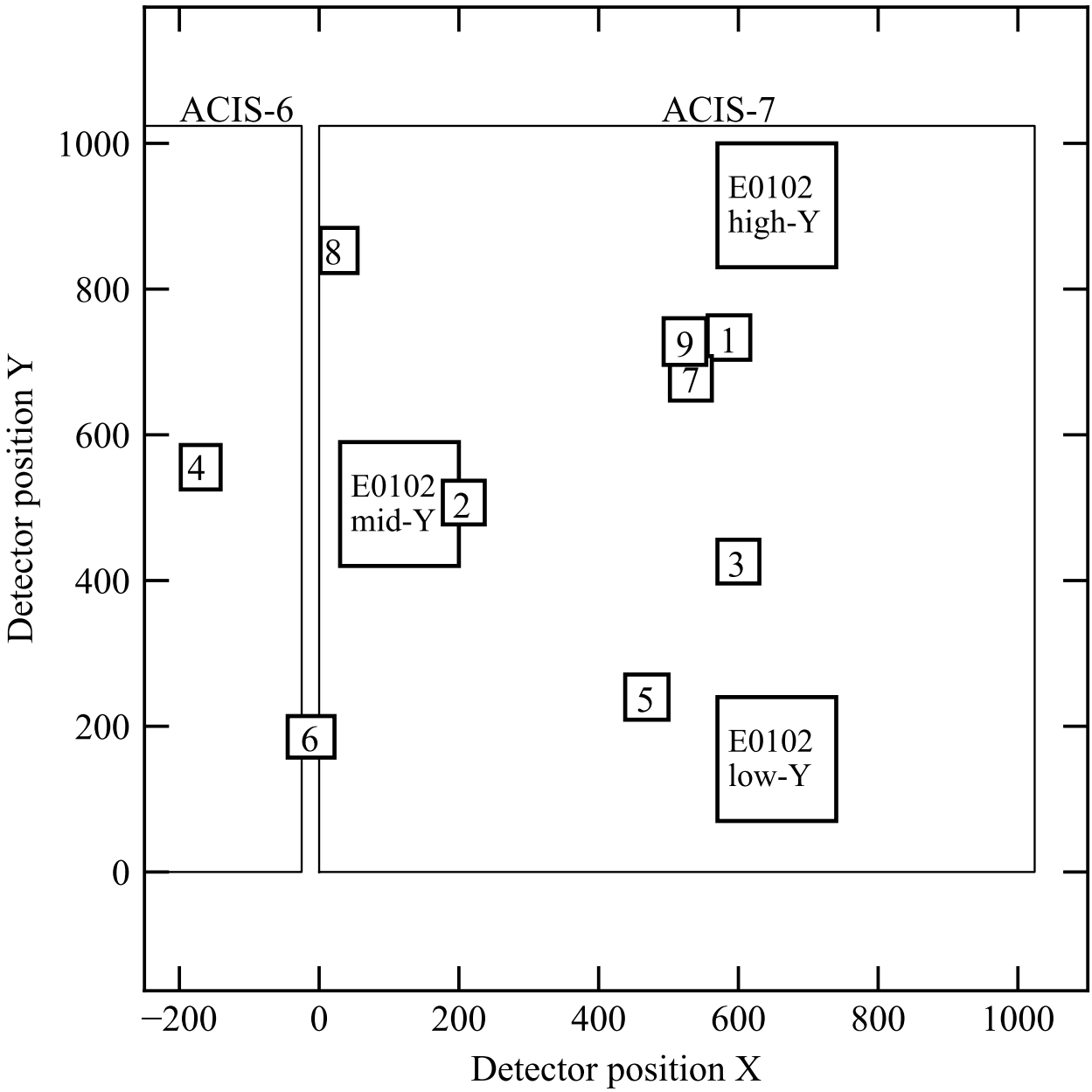

Figure6.9 The hot spot and E0102 detected positions on the ACIS are shown. The small squares surrounding the numbers indicates the hot spot position in each epoch. The three middle squares indicate the E0102 positions of low, mid and high-Y. The large squares of thin solid line indicates the ACIS chips 6 and 7.

and outer radii of 12 and 20 arcsec for the source and background regions, respectively. We simultaneously fitted spectra from the 9 epochs with the absorbed power-law model as same as for the *XMM-Newton* sepctrum. The model well reproduced the spectrum with the best fit chi-square statistics of χ^2/d.o.f.=375/388. The best fit parameters are summarized in Table 6.7. The derived parameters are consistent with the analysis of early *Chandra* data in Wilson et al. (2001).

For a simplification, we combined the spectra in epoch 1–9 with the `addascaspec` command. The combined spectrum is also well reproduced by the model as same as in simultaneous fitting. The best-fit parameters are

summarized in Table 6.7. There is no significant difference between the best-fit models for the simultaneous and combined fittings. We used the combined spectrum in the following analysis.

NuSTAR Spectrum

To reveal the hard X-ray property of the western hot spot, we analyzed the *NuSTAR* spectrum. As shown in Figure 6.7, we employed a circular regions with a radius of 50 arcsec, centered at the centroid of the brightness distribution of the western hot spot, and a rectangular region in the same detector chip for the source and background, respectively. We extracted the source and background spectra via the `nuproducts` script which also generates the response matrix functions and the auxiliary response files. Figure 6.12 shows the source and background spectra of the FPMA and FPMB. In both detectors, we see significant emission from the hot spot in the energy range of 3–20 keV.

We fitted the background subtracted spectra with the absorbed power-law model as same as for *XMM-Newton* and *Chandra* spectra. Figure 6.13 shows the background subtracted spectra and the best-fit models. The best-fit parameters are summarized in Table 6.7. The models well reproduce the spectra with χ^2/d.o.f. = 15.3/21 and 23.5/23 for FPMA and FPMB, although the FPMA spectrum prefers a slightly softer photon index of $\Gamma = 2.0 \pm 0.3$ to that of FPMB of $\Gamma = 1.6 \pm 0.4$. To investigate the spectral difference, we calculated the confidence contours between the flux and photon index, as shown in Figure 6.14. The parameters are consistent with each other to within a 68% confidence level. Therefore, there is no significant difference between FMPA and FMPB. Then, we performed a joint fitting. The best-fit parameters and confidence contours are shown in Table 6.7 and Figure 6.14, respectively. We confirmed that the joint fitting well reproduces the FPMA and FPMB spectrum with χ^2/d.o.f. = 42.3/44 and the best-fit parameters are consistent with those derived from individual fittings.

Broadband X-ray spectrum

Figure 6.15 shows the hot spot spectra obtained by *NuSTAR*, *XMM-Newton* and *Chandra*. The spectra are connected smoothly, as expected from Table 6.7 showing that the best-fit parameters are almost consistent among different satellites. Therefore, we performed a simultaneous fitting using all the data. The data cover wider energy range (0.2–20 keV) and have higher photon statistics than ever for this object. We simultaneously fitted the spectra by the absorbed power-law model with the fixed column density. The best-fit model well reproduced the spectrum with χ^2/d.o.f.=577/551, as shown in Figure 6.15. The derived best-fit parameters, summarized in Table 6.7, are almost consistent with the parameters derived from the individual spectrum.

In order to improve the fitting, we fitted the data with the same model by allowing the hydrogen column density to vary freely. The best-fit parameters are shown in Table 6.7. This model gives χ^2/d.o.f.=563/550, indicating a statistically significant improvement with a null hypothesis probability of 2×10^{-4} calculated from the *F*-test. The derived column density of $N_{\rm H}$=(4.6$\pm$0.5)$\times 10^{20}$ atom cm^{-2} is higher than the Galactic value from HI4PI Collaboration et al. (2016), while the others are statistically consistent with the case of the fixed column density. In addition, the spectral break repoted in Hardcastle et al. (2016) is not seen in the spectrum. The break is considered to be artificially caused by the *Chandra* low-energy spectrum obtained, including the effect from the molecular contamination.

As an advanced investigation, we searched for a spectral curvature. If the X-ray spectrum originates from an electron synchrotron emission, a high-energy exponential cut-off corresponding to the maximum energy of electrons is naturally expected. We thus fitted the spectrum with a simple cut-off power-law model of `tbabs*cutoffpl`. As a result, no cut-off energy is required below 400 keV. The energy of 400 keV is far above the energy coverage

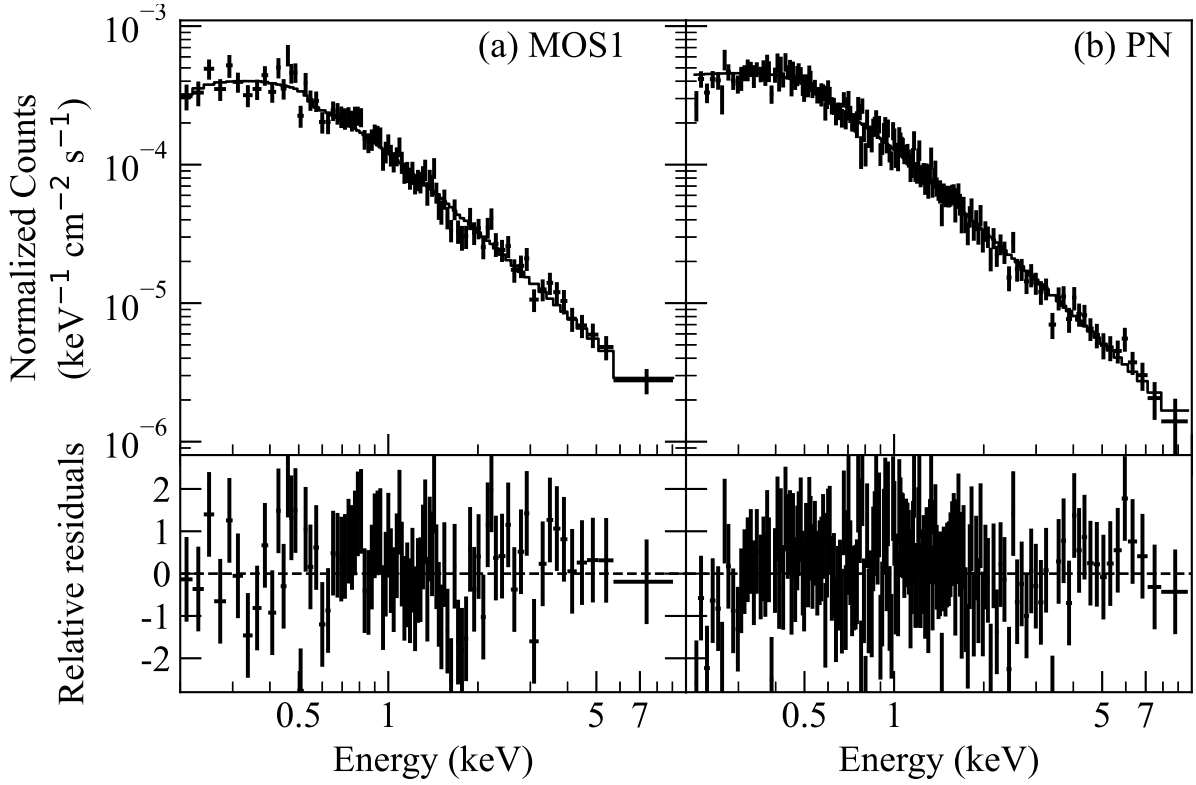

Figure6.10 The source and background spectrum are shown as crosses and squares, respectively. The left and right panels indicate MOS1 and PN, respectively.

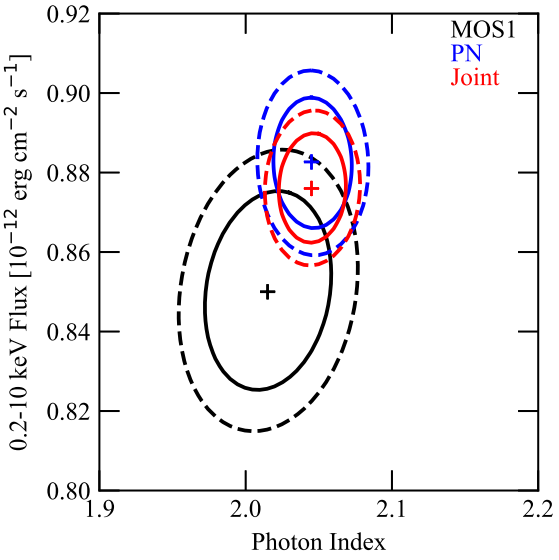

Figure6.11 The confidence contours for the 0.5-7 keV flux and photon index of the MOS1(black), PN(blue) and MOS1 and PN jointed(Red) spectrum fitting. The solid and dashed lines indicate 68% and 90% confidence level, respectively. The crosses indicate best-fit parameters.

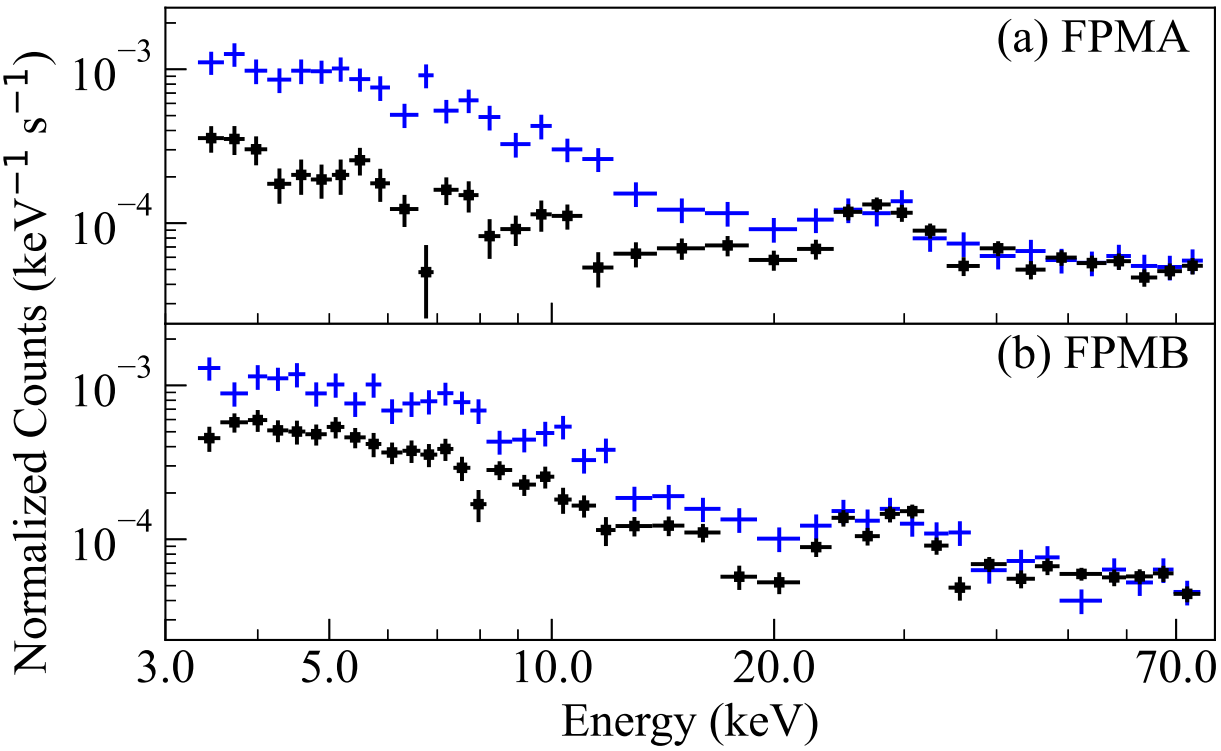

Figure6.12 The source and background spectrum are shown as crosses and squares, respectively. The upper and lower panel indicate FPMA and FPMB, respectively.

of our data (0.2–20 keV), and is also model dependent. Therefore, it would be reasonable to adopt 20 keV as our conservative lower limit of the cut-off energy.

It is interesting to note the analogy with studies of SNRs. Although X-ray synchrotron spectra in SNRs look similar to that observed in the Pictor A's western hot spot, the they are interpreted differently — they are generally believed to be tails of power-law emission with an exponential cut-off below $\sim$1 keV (see reviews, Helder et al. (2012); Vink (2012) and reference therein). For a recent example, Nagayoshi et al. (2021) revealed a power-law spectrum up to 30 keV, similar to the hot spot, and showed that it is reproduced by a power-law with an exponential cutoff at $\sim$0.5 keV. Therefore, one may think that the same interpretation could be applicable to the hot spot. However, the X-ray spectrum cannot be represented by the model of `tbabs*srcut`, which is the simple cut-off power-law model often used for SNRs, if we assume a cut-off energy below 20 keV. Hence, the cut-off energy would be higher than 20 keV for this model, too.

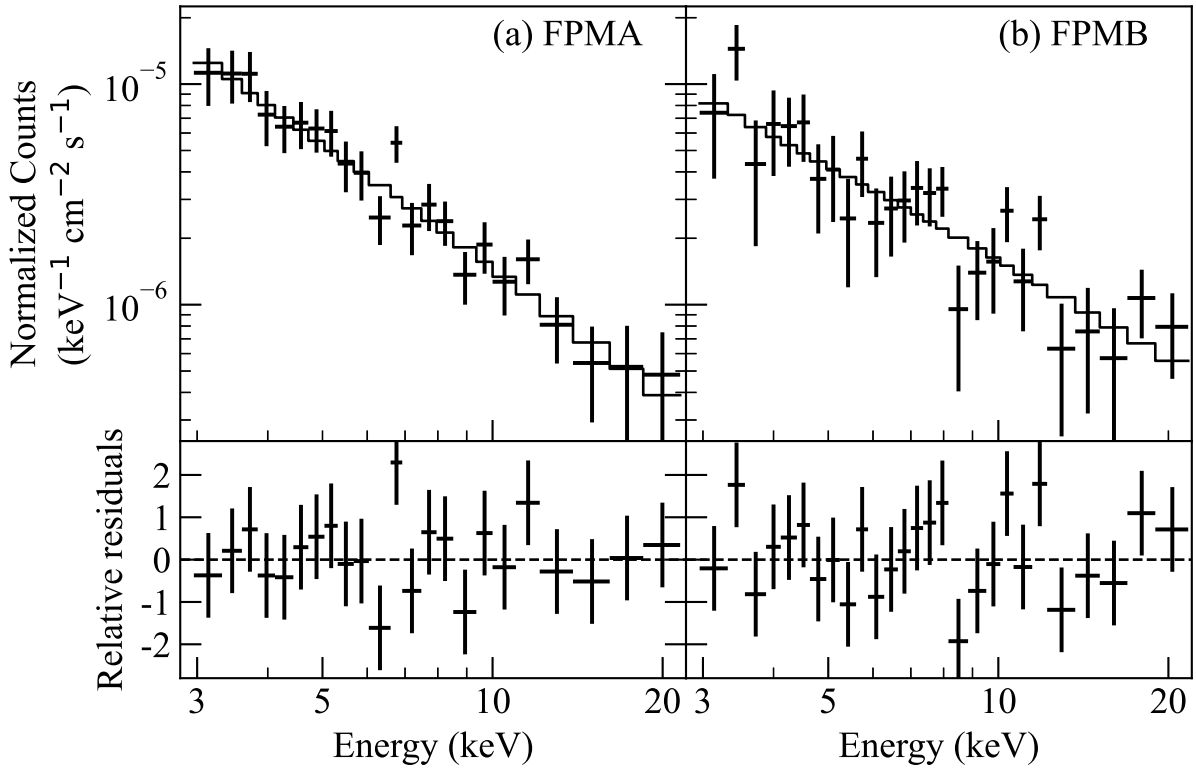

Figure6.13 The background subtracted spectrum and folded best-fit model are shown as the cosses and solid line,respectively. The right and left panel indicate FPMA and FPMB, respectively.

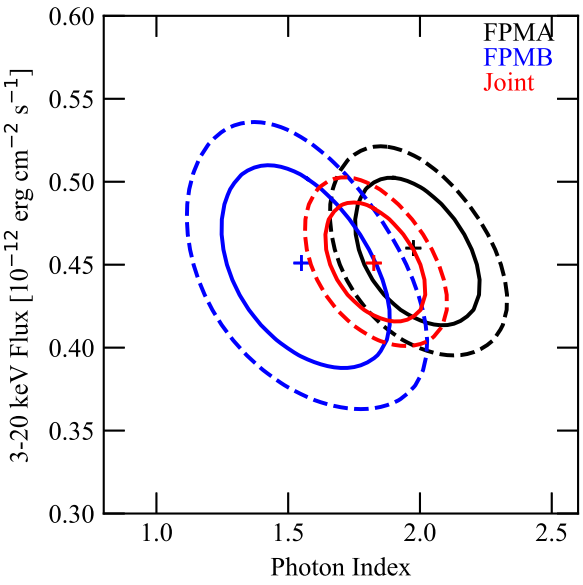

Figure6.14 The confidence contours for the 3-20 keV flux and photon index of the FPMA(black), FPMB(blue) and FPMA and FPMB jointed(Red) spectrum fitting. The solid and dashed lines indicate 68% and 90% confidence level, respectively. The crosses indicate best-fit parameters.

Table6.7 Best-fit parameters and 90% confidence error of each detector spectrum.

Instruments	Fitting range	Total Flux[a]	Common Flux[b]	Γ^c	$N_{\rm H}{}^d$	χ^2/d.o.f.
NuSTAR	3-20 keV					
FPMA		0.46±0.05	0.20±0.03	2.0±0.3	3.6 (fixed)	15.0/21
FPMB		0.45±0.06	0.16±0.03	1.6±0.4	3.6 (fixed)	23.5/23
FPMA+B		0.45±0.04	0.18±0.02	1.8±0.2	3.6 (fixed)	42.3/44
XMM-Newton	0.2-10 keV					
MOS1		0.86±0.03	0.18±0.01	2.02±0.05	3.6 (fixed)	97/90
PN		0.89±0.02	0.181±0.009	2.05±0.03	3.6 (fixed)	197/181
MOS1+PN		0.88±0.02	0.181±0.007	2.04±0.03	3.6 (fixed)	290/268
Chandra	1.5-7.0 keV					
ACIS (joint)		0.345±0.007	0.185±0.006	2.07±0.04	3.6 (fixed)	375/388
ACIS (merged)		0.347±0.007	0.185±0.006	2.09±0.04	3.6 (fixed)	226/235
All	0.2-20 keV	1.05±0.01	0.189±0.004	2.02±0.02	3.6 (fixed)	577/551
	0.2-20 keV	1.07±0.02	0.185±0.004	2.07±0.03	$4.6^{+0.5}_{-0.5}$	563/550

aUnabsorbed flux within fitting range in the unit of 10^{-12} erg s^{-1} cm^{-2}.

b Unabsorbed flux within 3-7 keV in the unit of 10^{-12} erg s^{-1} cm^{-2}

c Photon Index of power-law model.

d Hydrogen column density in unit of 10^{20} atom cm^{-2}

6.2.7 Low energy spectrum

Figure 6.16 shows the UV spectrum of the hotspot obtained from the OM source catalog. The spectrum indicates the power-law like shape and then I fitted it. As the best-fit model, the flux at 4 eV and energy index are obtained as $(4.3 \pm 0.2) \times 10^{-13}$ erg s^{-1} cm^{-2} and 1.4 ± 0.1, respectively. The model seems well reproduce the spectrum but, the obtained chi-square of χ^2/d.o.f=13/3 is not enough to be accepted in statistic. There may remain systematic errors or a more preferred model.

To investigate the broadband low energy spectrum, we compiled the radio to UV spectrum and modeled it. Figure 6.17 shows the radio to UV SED of the hotspot. The radio to optical data are taken from literature (Isobe et al. 2020 and reference therein). The radio spectrum ranging from 10^{-6} to 10^{-3} eV shows a power-law like shape. The infrared spectrum exceeds the extrapolation of the radio one. A additional emission in infrared band is suggested in Isobe et al. (2017) and Isobe et al. (2020). The optical spectrum in literature seems smoothly connect to the UV one obtained from the OM. Therefore I considered them as same component. The optical to UV emission shows a softer spectrum than radio one.

To reproduce the spectrum by focusing on the optical to UV spectral shape, I adopted the power-law model with some features at high-energy-termination. I fitted the spectrum with cut-off and broken power-law models. The best-fit models and parameters are shown in Figure 6.17 and in Table 6.8, respectively. The spectrum clearly prefer the broken power-law model to the cut-off power-law one. The index change is obtained as $\Delta\alpha \simeq 0.65$. I tried to fit with it in case of continuous energy injection as $\Delta\alpha = 0.5$ and obtained the worth statistics of χ^2 = 82 than the free fit.

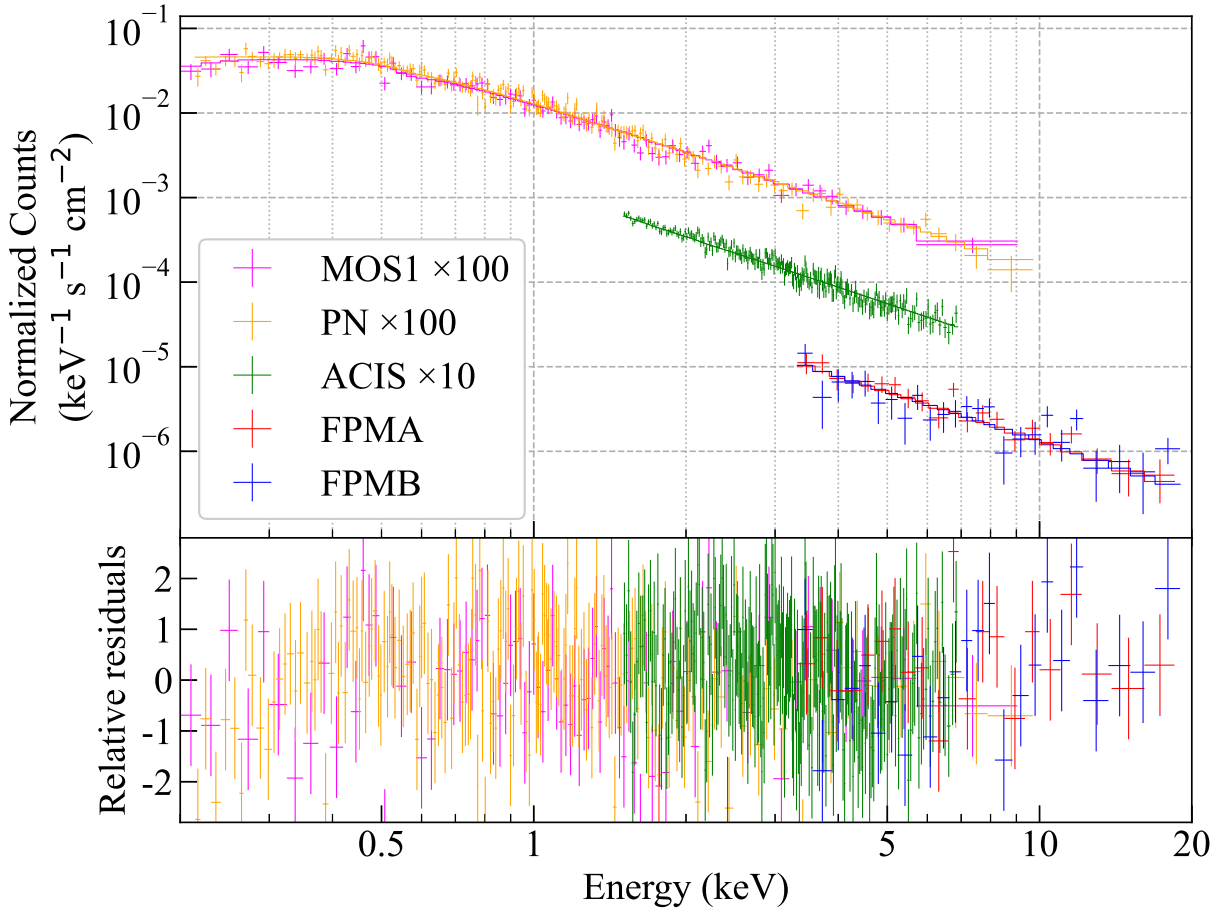

Figure6.15 Spectrum, folded best-fit absorbed power-law model and relative residuals of FPMA(red), FPMB(blue), ACIS(green), MOS1(magenta) and PN(orange) are shown. For only visibility, the counts of MOS1 and PN are 100 times scaled and counts of ACIS are 10 times scaled.

Table6.8 Best fit parameters for low-energy spectrum of Pictor A western hotspot

Model	Flux at 10^{-5} eV	$\alpha_{\rm radio}$	$E_{\rm cut}$ or $E_{\rm br}$	$\alpha_{\rm UV}$	χ^2/d.o.f.
Cut-off PL	9×10^{-9} (fixed)	0.745 (fixed)	1.9 ± 0.2 eV	-	281/12
Broken PL	9×10^{-9} (fixed)	0.745 (fixed)	0.34 ± 0.03 eV	1.4 ± 0.03	38/12

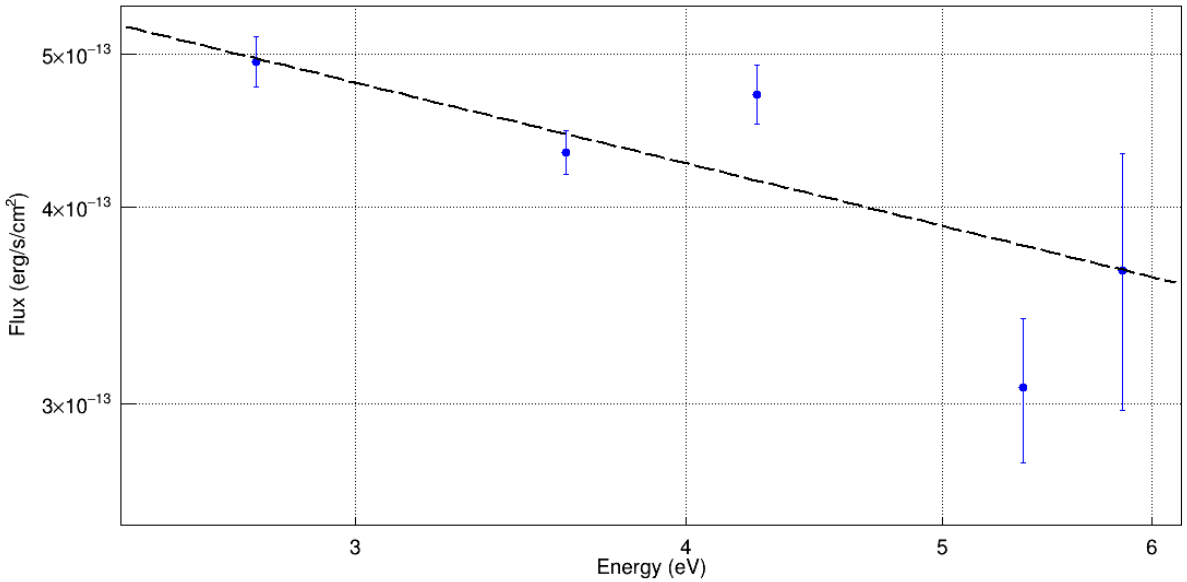

Figure6.16 The blue filled circles indicate the flux in OM 5 bands. The dashed line indicates the best-fit power-law model

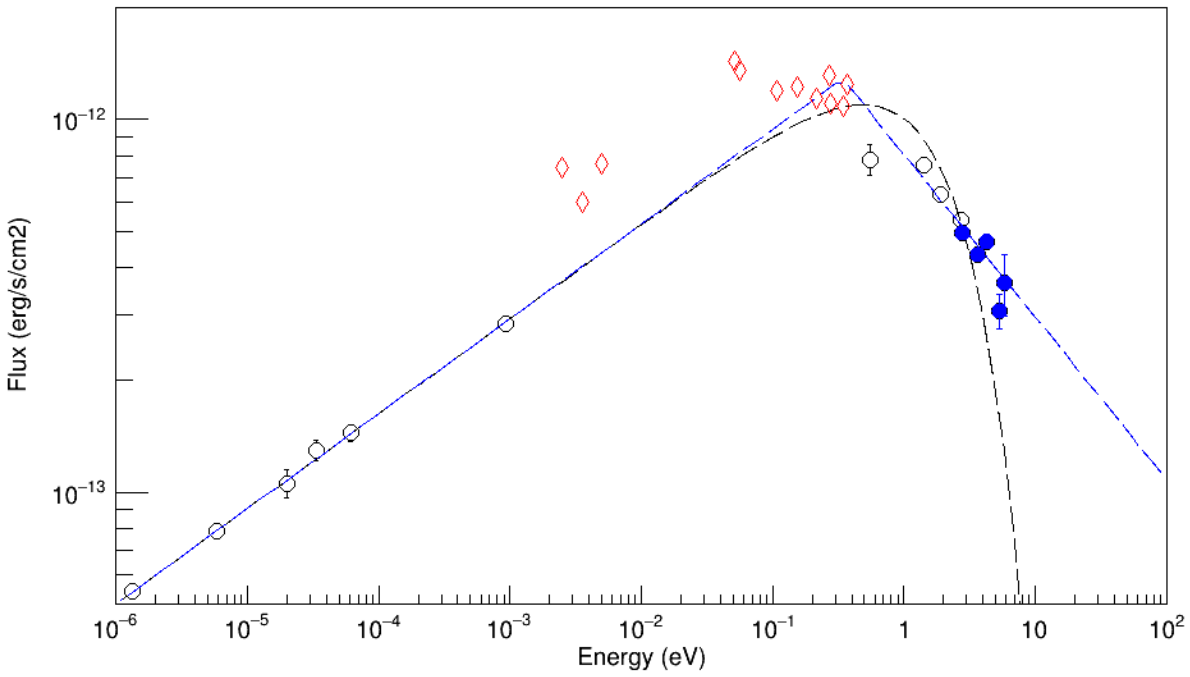

Figure6.17 The radio to UV spectrum of the Pictor A western hotspot. The blues filled circled, black open circles indicates the radio to optical and UV spectrum, respectively. The red open diamonds indicates the infrared spectrum, which ignored in the fitting. The dashed blue and black lines are the best fit model of broken power-law and cut-off power-law, respectively.

Chapter 7.

Disscusion

7.1 SED of Cygnus A hotspot

7.1.1 FIR Evidence of the cooling break

We discovered the FIR emission associated with the hot spot D, located at the east-jet terminal of the radio galaxy Cygnus A on the 70-350 μm images obtained by the *Herschel*/SPIRE and PACS. This is the second hot spot detected in the FIR range after the west hot spot of Pictor A (Isobe et al. 2020). After subtracting the contamination from the hot spot E, the FIR spectrum of the hot spot D is revealed to be consistent with the extrapolation from the radio PL spectrum. Therefore, the FIR emission is naturally attributed to the synchrotron emission from the same electron population producing for the radio emission.

In the radio to FIR range, the spectral energy index is derived as $\alpha \simeq 1.1$. As is pointed out by Stawarz et al. (2007), this spectral slope is explained by the diffusive shock acceleration (Bell 1978) operated at the hot spot, where some possible effects including relativistic one and/or magnetic-field configurations are considered. The synchrotron spectral shape at the higher frequency end depends on physical conditions associated with the acceleration region. Several models, including a simple one-shot energy-injection one, exhibit a high-frequency cut-off at the frequency corresponding to the maximum energy of the accelerated electrons. In contrast, the diffusive shock acceleration under a continuous injection (Meisenheimer et al. 1989; Carilli et al. 1991) predicts a spectral break with $\Delta\alpha = 0.5$ due to radiative cooling, in addition to the high-frequency cut-off. By filling the gap between the radio and NIR bands with the FIR data, we, for the first time, confirmed that the BPL model with $\Delta\alpha = 0.5$ better reproduces the observed synchrotron spectrum of the object than the CPL one. This indicates that the diffusive shock acceleration under the continuous energy injection is the dominant acceleration process in the hot spot D.

Previous studies tried to estimate the cooling break frequency of the hot spot D, though it was not conclusive. Carilli et al. (1991) proposed the break feature in the GHz range as the cooling break. However, theoretical studies pointed out that the cooling break at higher frequency than GHz is preffered in hot spots (e.g., Kino and Takahara 2004). In addition, Stawarz et al. (2007) clearly demonstrated that the GHz break feature does not represent the cooling break, since they precisely evaluated the spectral index change at the GHz feature as $\Delta\alpha \simeq 0.8$, which is inconsistent with the cooling break (i.e., $\Delta\alpha = 0.5$), by re-analysing the high-resolution radio data. Instead, Stawarz et al. (2007) assumed the cooling break at the frequency of $\nu_{\rm br} = 0.5 \times 10^{12}$ Hz to reproduce the spectrum they obtained. However, it was unable to justify this assumption because the frequency falls in the spectral gap between the radio and NIR ranges. We overcame this difficulty by introducing the newly obtained FIR data with

Herschel. Thus, we have succeeded in directly measuring the cooling break as $\nu_{\rm br} = 2.0^{+1.2}_{-0.8} \times 10^{12}$ Hz.

7.1.2 Magnetic-field estimation

In this section, we evaluate the magnetic field strength B in the hot spot D. First, we constrain the magnetic field strength B as a function of the observed radius of the hot spot, R. Next, we re-evaluate the observed X-ray spectrum with the Synchrotron-Self-Compton (SSC) process to obtain an independent constraint on B and R from the cooling break. Finally, by combining these two considerations, we precisely determine the magnetic field strength in the hot spot D.

Constraint from the cooling break frequency

From the cooling break frequency, we measure the magnetic field strength B as the function of the radius R. The cooling break is determined by mutual balance between an electron radiative cooling time scale, $t_{\rm syn} = \frac{6\pi m_{\rm e} c}{B^2 \sigma_{\rm T} \gamma}$ and an adiabatic loss time scale, $t_{\rm ad} = \frac{2R}{\beta c}$, where $m_{\rm e}$, c, $\sigma_{\rm T}$, γ and β are the electron rest mass, speed of light, Thomson cross section, electron Lorentz factor, and downstream flow velocity behind the shock in the shock frame. Here, for simplicity, the Compton cooling is neglected based on the relative observed strength of the synchrotron and SSC components. Because the two time scale becomes equal to each other at the cooling break, the Lorentz factor at the cooling break is given by

$$\gamma_{\rm br} = \frac{3\pi m_{\rm e} c^2 \beta}{\sigma_{\rm T} R B^2} \tag{7.1}$$

(Inoue and Takahara 1996). For high energy electrons above the cooling break, $\gamma > \gamma_{\rm br}$, the synchrotron spectral slope changes by $\Delta\alpha = 0.5$, assuming that the energy injection is constant in time. The synchrtron frequency corresponding to the break Lorentz factor is derived as $\nu_{\rm br} = \frac{3eB\gamma_{\rm br}^2}{4\pi m_{\rm e} c}$, where e is the elementary charge. Thus, the magnetic field B is estimated from the break frequency as

$$B = \left(\frac{27\pi m_{\rm e} e c^3 \beta^2}{4\sigma_{\rm T}^2} R^{-2} \nu_{\rm br}^{-1} \right)^{1/3} \tag{7.2}$$

$$\simeq 190\ \mu{\rm G} \times \left(\frac{\beta}{1/3} \right)^{\frac{2}{3}} \left(\frac{R}{1\ {\rm kpc}} \right)^{-\frac{2}{3}} \left(\frac{\nu_{\rm br}}{10^{12}{\rm Hz}} \right)^{-\frac{1}{3}}. \tag{7.3}$$

This method was successfully applied to estimate the magnetic field in blazars (e.g., Inoue and Takahara 1996; Kataoka et al. 2000) and hot spots, including the west hot spot of Pictor A (Isobe et al. 2020).

By substituting the observed break frequency, $\nu_{\rm br} = 2.0^{+1.2}_{-0.8} \times 10^{12}$ Hz, in Equation 7.3, we derive the magnetic field as a function of the radius as,

$$B \simeq 150^{+30}_{-20} \times \left(\frac{R}{1\ {\rm kpc}} \right)^{-\frac{2}{3}} \mu{\rm G}. \tag{7.4}$$

Here, we employed the theoretical value of the downstream velocity in a shock rest frame in the ideal relativistic shock as $\beta = 1/3$ (Kirk and Duffy 1999). The area enclosed by the thick blue lines in Figure 7.1 indicates the acceptable magnetic field given by Equation 7.4.

In order to further constrain the magnetic field from Equation 7.4, we evaluate the radius of the object from the previous studies (e.g., Harris et al. 1994; Wilson et al. 2000; Kino and Takahara 2004; Stawarz et al. 2007). We conservatively adopt the radius range of 0.8 kpc $< R < 1.6$ kpc, which roughly covers the radius estimations in the previous studies. The lower limit corresponds to the radius adopted in Stawarz et al. (2007) based on the VLA high-resolution observation (Perley et al. 1984), while the upper one was derived from the X-ray image

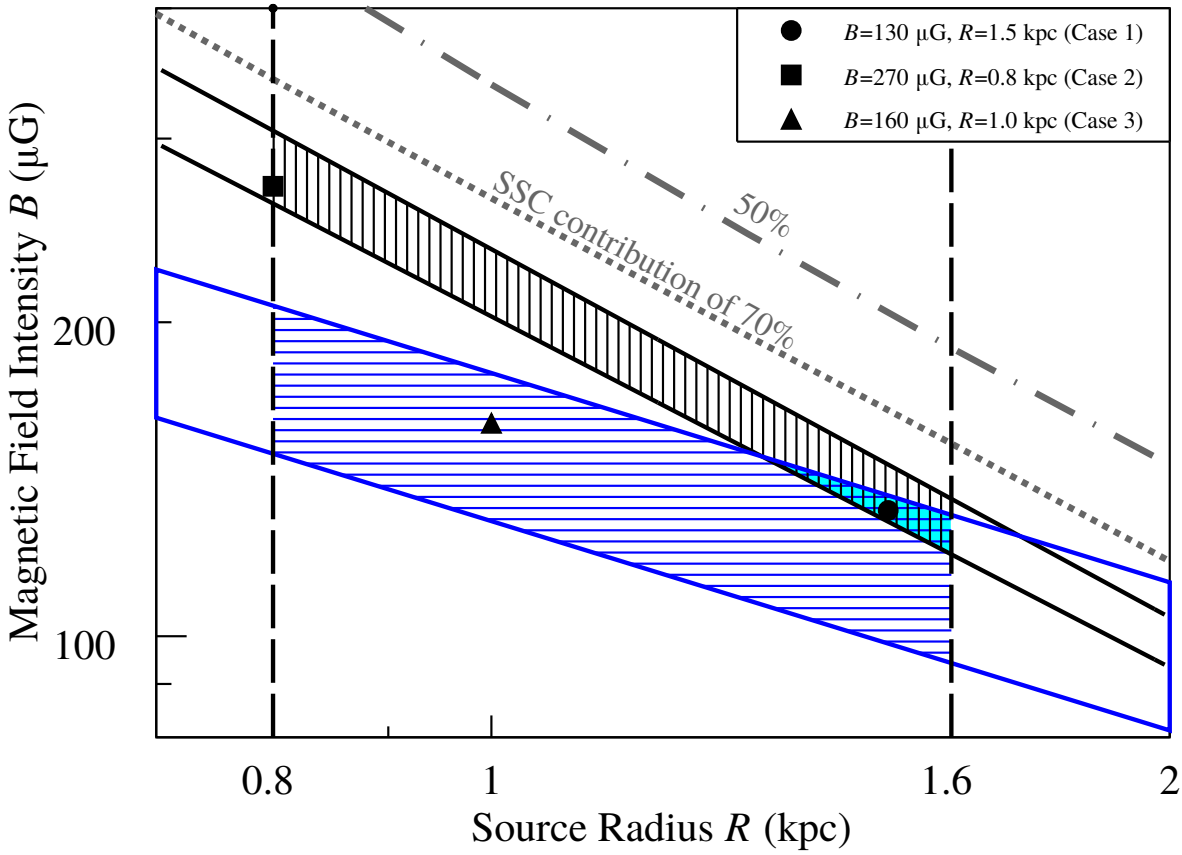

Figure7.1 The magnetic field B and the radius R for the hotspto D. The vertical dashed lines indicate the radii of $R = 0.8, 1.6$ kpc. The region enclosed by the blue solid line is the constraint from the FIR cooling break. The parallel blue striped region indicates the constraint from the cooling break and the radius. The region between the black solid lines corresponds to the constraint from the SSC X-ray flux. The vertical black striped region indicates the constraint from the SSC X-ray flux and the radius. The cyan filled region indicated the parameters satisfying both constraint from the cooling break and the SSC X-ray flux. The black filled circle associate to Case 1 indicates the parameters of B=150 μG, R=1.3 kpc. The black filled square associated to Case 2 and indicate the parameters of B=270 μG and R=0.8 kpc adopted in Stawarz et al. 2007. The black filled triangle associated to Case 3 and indicate the parameters of B=160 μG and R=1.0 kpc. The grey dash-dotted and dotted lines indicates the conditions which SSC flux reproduces the 50 per cent and 70 per cent of observed X-ray flux, respectively.

with *Chandra* (Wilson et al. 2000). The horizontally hatched area in Figure 7.1 shows the magnetic field for the adopted radius range. Thus, the magnetic field is determined as $B = 90$–210 μG by using the cooling break.

Constraint from the X-ray spectrum

We performed the Synchrotron-Self-Compton (SSC) modelling (Band and Grindlay 1985) to the observed X-ray spectrum of the hot spot D, in order to constrain the magnetic field independently from the cooling break. The SSC model is widely adopted to interpret the X-ray spectra of numbers of hot spots, and to constrain their magnetic field (Wilson et al. 2000; Hardcastle et al. 2004; Kino and Takahara 2004; Kataoka and Stawarz 2005). In the SSC process, the flux ratio of the synchrotron to SSC components depends on the magnetic field and the radius of the source. Stawarz et al. (2007) estimated the magnetic field of the hot spot D as $B = 270$ μG, by applying the

SSC model to its X-ray spectrum for the fixed radius of R=0.8 kpc. We, here, re-modelled the X-ray spectrum of the object by the SSC process to constrain the magnetic field for the radius range of 0.8 kpc <R< 1.6 kpc, as we adopted in the previous subsection.

We compiled the broadband SED of the hot spot D, as shown in Figure 7.2. The FIR data are those we obtained in section 6 (See Table 6.3). The radio, NIR, and X-ray data are taken from Stawarz et al. (2007), in which the hot spot D is resolved from the hot spot E with the high-resolution images. The synchrotron spectrum of this object is measured in a wide frequency range between the radio and NIR bands. As mentioned in section 7.1.1, the spectrum appears to exhibit a low-frequency cut-off feature around 10^9 Hz. Although the origin of this feature is under deviate (Carilli et al. 1991; McKean et al. 2016; Stawarz et al. 2007), we did not discuss it any further in the present paper. Thus, we only examine the synchrotron spectrum above the minimum frequency of $\nu_{\rm min} = 1.4 \times 10^9$ Hz. In contrast, the synchrotron spectrum shows the high frequency cut-off, of which the frequency is determined as $\nu_{\rm cut} = (1.2 \pm 0.3) \times 10^{13}$ Hz, in addition to the cooling break, as discussed in section 6.1.3. This cut-off is attributed to the maximum electron energy. The X-ray spectrum significantly exceeds the extrapolation of the radio-to-NIR synchrotron spectrum. Therefore it is thought to be produced via the SSC process.

We calculated the synchrotron and SSC spectra to reproduce the observed radio-to-X-ray SED For the calculation, the open source package of NAIMA versioin 0.9.1 (Zabalza 2015) was utilised. Based on the observed shape of the synchrotron spectrum in the range of $\nu > \nu_{\rm min}$, the input electron spectrum is assumed to be simply described by a broken power-law model as shown below;

$$N_{\rm e}(\gamma) = N_0 \begin{cases} \left(\dfrac{\gamma}{\gamma_{\rm min}}\right)^{-p} & \text{for } \gamma_{\rm min} \leq \gamma < \gamma_{\rm br} \\ \left(\dfrac{\gamma_{\rm br}}{\gamma_{\rm min}}\right)^{-p} \times \left(\dfrac{\gamma}{\gamma_{\rm br}}\right)^{-(p+1)} & \text{for } \gamma_{\rm br} \leq \gamma \leq \gamma_{\rm max} \\ 0 & \text{for otherwise} \end{cases} \tag{7.5}$$

where N_0, p, $\gamma_{\rm min}$, and $\gamma_{\rm max}$ are the normalisation in the unit of the electron number per unit Lorentz factor, the spectral energy index, the minimum and maximum electron Lorentz factors, respectively. Thus, it is necessary to specify the seven parameters to simulated the overall spectrum; i.e., B, R, N_0, p, $\gamma_{\rm min}$, $\gamma_{\rm br}$ and $\gamma_{\rm max}$.

Through the following procedures, we check if a certain pair of B and R is possible to reproduce the observed SED shown in Figure 7.2. Based on the synchrotron energy index of $\alpha = 1.07$ between the radio and FIR bands determined in section 6.1.3, the electron spectral index of $p = 2\alpha + 1 = 3.14$ is adopted. The minimum and cut-off synchrotron frequencies, $\nu_{\rm min}$ and $\nu_{\rm cut}$ respectively, are transformed into the minimum and maximum Lorentz factors, $\gamma_{\rm min}$ and $\gamma_{\rm max}$, as $\gamma = \sqrt{\frac{4\pi m_{\rm e} c \nu}{3qB}}$. In order to keep consistency to B and R, we adopted the break Lorentz factor calculated from Equation 7.1 instead of the observed value. We determine the electron normalisation N_0 so that the simulated synchrotron flux reproduces the observed one as $F_{10\ \rm GHz} = 27$ Jy at 10 GHz (Stawarz et al. 2007). With these parameters, we compared the SSC model spectrum with the observed X-ray spectrum. If the calculated flux agrees with the observed X-ray one at 1 keV, $F_{\rm X} = 47.0 \pm 5.9$ nJy (Stawarz et al. 2007), the input B-R pair is regarded as viable. We iterate these procedures for a wide range on the B-R plane. We show the synchrotron and SSC spectra for some representative values of B and R (i.e., Cases 1–3) in Figure 7.2 and tabulated the parameters in Table 7.1.

The area enclosed by the two thick black solid lines in Figure 7.1 indicates the acceptable values of the magnetic field and radius. As discussed in Section 7.1.2, we adopted the additional constraint on the radius as 0.8 kpc $< R <$ 1.6 kpc. Thus, we finally obtained the black vertically hatched area in Figure 7.1, within which the observed 10 GHz radio and 1 keV X-ray fluxes are consistently described with the synchrotron and SSC

Table7.1 Parameters for the calculation of synchrotron and SSC spectra

case	B μG	R kpc	p	N_0 particle per Lorentz factor	$\gamma_{\rm min}$	$\gamma_{\rm max}$	$\gamma_{\rm br}$
Case 1	130	1.5	3.14	6.4×10^{56}	$1.5{\times}10^3$	$1.4{\times}10^5$	$4.9{\times}10^4$
Case 2	270	0.8	3.14	4.4×10^{56}	$1.1{\times}10^3$	$9.9{\times}10^4$	$2.1{\times}10^4$
Case 3	160	1.0	3.14	5.7×10^{56}	$1.4{\times}10^3$	$1.3{\times}10^5$	$4.9{\times}10^4$

components, respectively.

Magnetic field determination

By combining the investigation into the cooling break and the SSC modelling to the X-ray spectrum, shown in sections 7.1.2 and 7.1.2 respectively, we tightly constrained the magnetic field strength in the hot spot D. The derived B-R conditions from the individual considerations overlap with each other in the blue filled region on Figure 7.1, showing the magnetic field strength of $B = 120$–150 μG for the radius $R = 1.3$–1.6 kpc. This is the most stringent magnetic-field constraint ever achieved for hot spots of radio galaxies (e.g., Hardcastle et al. 2004; Kataoka and Stawarz 2005).

In order to visually validate the magnetic-field estimation, the synchrotron and SSC model spectra are plotted in Figure 7.2 for three representative cases (Cases 1, 2, and 3). As shown with the filled circle in Figure 7.1, Case 1 (B=130 μG and R=1.5 kpc) simultaneously satisfies the two constraints. Therefore, the observed cooling break and X-ray flux are successfully reproduced by the synchrotron and SSC model components, respectively, as displayed with the thick solid lines in Figure 7.2. Case 2 (B=270 μG and R=0.8 kpc), plotted with the filled box in Figure 7.1, is located within the acceptable region to the X-ray spectrum, but outside the region to the cooling break. The parameters of Case 2 were adopted in Stawarz et al. (2007). The dashed line in Figure 7.2 clearly shows that the SSC model flux agrees with the observed X-ray one, although the cooling break frequency predicted by the model is lower than the observed value. The filled triangle in Figure 7.1 points to the parameters of Case 3 ($B = 160$ μG and $R = 1.0$ kpc), which only meets the cooling break condition. Thus, the simulated synchrotron spectrum is compatible with the observed cooling break, though the SSC model overestimates the X-ray flux, as depicted with the dashed line in Figure 7.2.

With the cooling break properly taken into account in the SSC model, we have succeeded in strongly constraining the magnetic field in the hot spot D of Cygnus A (B=120–150 μG). If this method is systematically applied to the other hot spots, their magnetic field is expected to be precisely measured. In fact, a number of hot spots are suggested to exhibit the cooling break in the FIR range, because their magnetic field and radius are typically evaluated in the range of $B = 100$–500 μG and $R = 0.3$–3 kpc (e.g Kataoka and Stawarz 2005; Zhang et al. 2018). In addition, Cheung et al. (2005) predicted that the cooling break is located around the FIR band for three optical hot spots, by simply connecting the radio and optical spectra with the broken PL model. Therefore, future FIR studies gives a powerful tool to evaluate the physical condition in the hot spots, by detecting the cooling break.

7.1.3 Validity of the SSC scenario

When we estimated the magnetic field strength of the hot spot D in Section 7.1.2, we simply assumed that all the observed X-ray flux is attributable to the SSC emission. Strictly speaking, there is no physical rationale for this

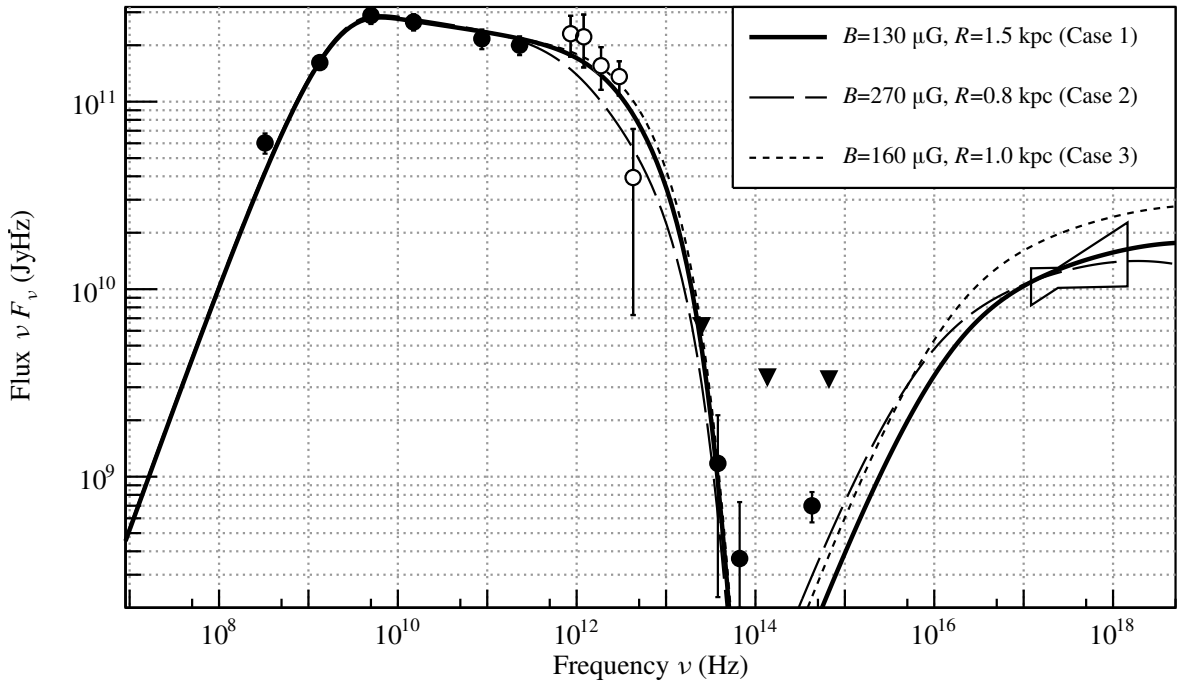

Figure7.2 The broadband SED of the hot spot D and the SSC model calculated in section 4.2.2. The open circle indicates the FIR spectrum obtained in this work. The black filled circles and the black filled triangles are data points and upper limits(Stawarz et al. 2007 and references there in). The solid line indicates the SSC model on the parameters associated to Case 1 of B=130 μG and R=1.5 kpc. The dashed line indicates the model on the parameters associated to Case 2 of B=270 μG and R=0.8 kpc. The dotted line indicates the model on the parameters associated to Case 1 of B=160 μG and R=1.0 kpc.

assumption, although it is widely applied to X-ray studies of hot spots (Hardcastle et al. 2004; Kataoka and Stawarz 2005; Zhang et al. 2018). Actually, it is suggested that the X-ray spectrum of some optical hot spots is contaminated by other spectral components, including the synchrotron emission from an additional electron population (Wilson et al. 2001; Hardcastle et al. 2007; Kraft et al. 2007; Perlman et al. 2010). As a by-product of the cooling break determined from the FIR data, we successfully quantitatively restrict the contribution of components different from the SSC one to the observed X-ray spectrum of the hot spot D.

Compact synchrotron emitting sources, including the hot spots, are inevitably accompanied by the SSC emission. However, the SSC contribution to the observed X-ray spectrum is thought to be reduced by the contamination from alternative emission processes. The SSC model flux is predicted to scale as roughly $F_{\rm SSC} \propto B^{-2}$, as far as the synchrotron flux is fixed at the observed value. Therefore, a higher fraction of the alternative spectral components is inferred to enhance the magnetic field estimation, and hence, to shift upward the B-R region on Figure 7.1 allowed by the SSC model (i.e., the vertically hatched area).

The dotted and dash-dotted lines in Figure 7.1 represent the B-R relation, derived by a manner similar to that

adopted in Section 7.1.2, for the cases where the SSC model reproduces 70 and 50 per cent of the observed X-ray flux, respectively. Such a small SSC contribution is clearly rejected from Figure 7.1, because these two lines do not intersect the horizontally hatched region obtained by the cooling break consideration. In order for the regions from the cooling break and SSC conditions to overlap with each other, we found that the SSC fraction of higher than ~ 98 per cent of the best-fit X-ray flux (i.e., 47 nJy) is required. In the case of the lowest acceptable SSC fraction of 98 per cent, the regions from the two conditions cross at the top-right corner of the horizontally hatched region in Figure 7.1, which corresponds to the magnetic field of $B = 130$ μG and the radius of $R = 1.6$ kpc, respectively.

In this way, we have put a very tight lower limit on the SSC contribution to the X-ray spectrum of the hot spot D in the radio galaxy Cygnus A, owing to the detection of the cooling break. This result strongly indicates that the SSC emission significantly dominates the X-ray spectrum of this object. If the cooling break is systematically detected in the other hot spots, the SSC scenario for the hot spots' X-ray spectrum is possibly justified with high reliability.

7.2 SED of Pictor A hotspot

7.2.1 Interpretation of the UV spectrum

The radio to UV spectrum is well reproduced by the broken power-law model. This strongly evidenced the contiunously injected the acceleration particles and the effective synchrotron cooling. Therefore, same as the Cygnus A hotspot D, the magnetic field strength is estimated. I adopted the break energy of $E_{\rm br} = 0.34 \pm 0.03$ eV obtained from the analysis. Then, the magnetic field is estimated as

$$B \simeq 30\ \mu\mathrm{G} \times \left(\frac{\beta}{1/3}\right)^{\frac{2}{3}} \left(\frac{R}{1\ \mathrm{kpc}}\right)^{-\frac{2}{3}} \left(\frac{E_{\rm br}}{1\mathrm{eV}}\right)^{-\frac{1}{3}} \tag{7.6}$$

$$\simeq 43 \pm 2\ \mu\mathrm{G} \times \left(\frac{R}{1\ \mathrm{kpc}}\right)^{-\frac{2}{3}}. \tag{7.7}$$

In the radio and optical high-resolution imaging, the hotspot size is estimated about 0.7 kpc.

7.3 Origin of the X-ray from Pictor A hot spot

7.3.1 Interpretation of the X-ray

The X-ray emission mechanism of the Pictor A western hot spot is under investigation since the first clear detection by *Chandra* in Wilson et al. (2001). The X-ray spectrum is brighter and harder than the extrapolation of the radio to optical synchrotron spectrum. Wilson et al. (2001) indicated that the SSC process is challenging to reproduce the spectrum. It is considered plausible that the X-ray originates from a synchrotron emission of the electrons different from that corresponding to the radio to optical emission (see, Wilson et al. (2001); Hardcastle et al. (2004)).

Furthermore, Tingay et al. (2008) proposed that X-rays originate from the fine structure around the radio brightness peak and Hardcastle et al. (2016) supported the scenario basis on the time scale of the flux decrease. However, we confirmed no strong evidence of the flux decrease. In additioin, the X-ray image obtained in detailed analysis in Thimmappa et al. (2020) shows the spatial offset between the X-ray brightness peak and the radio one. Therefore, the fine structure scenario is not favored. Alternatively, as mentioned in Thimmappa et al. (2020), the X-ray emitted from the shock front is plausible.

7.3.2 Accelerated electron energy distribution

Hot spots are believed to be the site of the particle acceleration via the relativistic shock and the possible ultra-high-energy cosmic-ray accelerator (Hillas 1984; Kotera and Olinto 2011). Therefore the observational electron spectrum of the hot spot is essential information for the relativistic shock study.

The X-ray observations in a wide energy range with high statistics revealed the featureless power-law spectrum within 0.2–20 keV. The spectrum indicates that the X-ray emitting electrons are not at the highest energy term (see Section 3). Therefore we estimated the X-ray emitting electron's spectral index (p), which is the important information of the acceleration process, from the X-ray energy index ($\Gamma = 2.07 \pm 0.03$) as $p = 2\Gamma - 1 = 3.14 \pm 0.06$.

To investigate the energy index of accelerated electrons, we should consider a synchrotron radiative cooling effect. If the cooling is effective in the observed energy range, the deribed energy index of p is changed from the accelerated electron's one of $p_{\rm acc}$ as $p = p_{\rm acc} + 1$ (see, Meisenheimer et al. (1989); Carilli et al. (1991)). When a radiative lifetime in the energy band is shorter than a dynamical time scale, the cooling become effective (see, Inoue and Takahara (1996); Kino and Takahara (2004)). The lifetime ($\tau_{\rm syn}$) in a photon energy of ($E_{\rm ph}$) is given from the magnetic field strength (B) as below

$$\tau_{\rm syn} \simeq 7 \times \left(\frac{E_{\rm syn}}{10\ {\rm keV}}\right)^{-\frac{1}{2}} \left(\frac{B}{300\ \mu{\rm G}}\right)^{-\frac{3}{2}} {\rm year}. \tag{7.8}$$

Here, we adopted the magnetic field of $B = 300\ \mu$G calculated from the radio to optical synchrotron spectrum under the assumption of the minimum or equipertition energy condition (Meisenheimer et al. (1989); Isobe et al. (2017)). On the other hand, considering that hot spots are generally as large as at least $L = 0.1$ kpc, the dynamical time scale is longer than $L/c \sim 300$ yr. Herer, c is the speed of light. Therefore, the cooling is almost certainly effective in X-ray band and the energy index of the accelerated electron is estimated as $p_{\rm acc} = p - 1 = 2.14 \pm 0.06$. The index is similar to the theoretical prediction in the diffusive shock acceleration under the strong schok condition of $p_{\rm acc} = 2$ or relativistic shock of $p_{\rm acc} \sim 2.4$ (see, e.g., Bell (1978); Spitkovsky (2008)).

Several authors (e.g, Wilson et al. (2001); Aharonian (2002)) already pointed out the same electron index of the hot spot. However, the low statistics due to only observation by *Chandra*, allowed the various X-ray spectral shape. Our study tightly determined the X-ray spectral shape and excluded the cut-off or cooling break feature in X-ray band.

In addition to the spectral index, the maximum electron energy ($E_{\rm e,max}$) is also important information. The maximum energy is observationally estimated from the synchrotron cut-off energy ($E_{\rm cut}$) as,

$$E_{\rm e,max} \simeq 40 \times \left(\frac{E_{\rm cut}}{20\ {\rm keV}}\right)^{\frac{1}{2}} \left(\frac{B}{300\ \mu{\rm G}}\right)^{-1} {\rm TeV}. \tag{7.9}$$

From our study, there is lower limit of the cut-off energy as $E_{\rm cut} > 20$ keV (see Section 3). Therefore, we put the lower limit for the maximum energy as $E_{\rm e,max} > 40$ TeV.

We compared the maximum electron energy to blazars, which have spectral and environmental similarities with hot spots. Some observational studies estimated the maximum electron energy as up to only a few TeV even in the TeV gamma-ray emitting blazars believed to have higher value among some types of blazar (see e.g., Inoue and Takahara (1996); Kataoka et al. (1999); Kino et al. (2002); MAGIC Collaboration et al. (2020)). Therefore the synchrotron X-ray in the hot spots may reflect the highest energy electron in the AGN jet system.

This study based on the hard X-ray detection by *NuSTAR*. To improve this study, we need to detect higher energy spectrum and or other hot spots than in this study. Due to both lower X-ray flux and smaller angular offset from the

nucleus in most of hot spots than in the Pictor A western hot spot, *NuSTAR* is probably hard to detect. We expects the future hard X-ray missions, which have better angular resolution and the sensitivity than those of *NuSTAR*, for example *FORCE*（Nakazawa et al. 2018）.

Reference

[1] Aharonian, F. A. 2002 "Proton-synchrotron radiation of large-scale jets in active galactic nuclei," *MNRAS* **332**, No. 1, 215-230, DOI: 10.1046/j.1365-8711.2002.05292.x.

[2] Anders, E. and Grevesse, N. 1989 "Abundances of the elements: Meteoritic and solar," *Geochimica Cosmochimica Acta* **53**, No. 1, 197-214, DOI: 10.1016/0016-7037(89)90286-X.

[3] Arnaud, K. A. 1996 "XSPEC: The First Ten Years," in Jacoby, G. H. and Barnes, J. eds. *Astronomical Data Analysis Software and Systems V* **101** of Astronomical Society of the Pacific Conference Series, 17.

[4] Band, D. L. and Grindlay, J. E. 1985 "The synchrotron-self-Compton process in spherical geometries. I - Theoretical framework," *ApJ* **298**, 128-146, DOI: 10.1086/163593.

[5] Bell, A. R. 1978 "The acceleration of cosmic rays in shock fronts - I.," *MNRAS* **182**, 147-156, DOI: 10.1093/mnras/182.2.147.

[6] Bentley, M., Haves, P., Spencer, R. E., and Stannard, D. 1975 "High resolution observations of extended radio sources at 1666 MHz," *MNRAS* **173**, 93P, DOI: 10.1093/mnras/173.1.93P.

[7] Carilli, C. L., Perley, R. A., Dreher, J. W., and Leahy, J. P. 1991 "Multifrequency radio observations of Cygnus A - Spectral aging in powerful radio galaxies," *ApJ* **383**, 554-573, DOI: 10.1086/170813.

[8] Cheung, C. C., Wardle, J. F. C., and Chen, T. 2005 "Discovery of Optical Emission in the Hot Spots of Three 3CR Quasars: High-Energy Particle Acceleration in Powerful Radio Hot Spots," *ApJ* **628**, No. 1, 104-112, DOI: 10.1086/430634.

[9] Eracleous, M. and Halpern, J. P. 2004 "Accurate Redshifts and Classifications for 110 Radio-Loud Active Galactic Nuclei," *ApJS* **150**, No. 1, 181-186, DOI: 10.1086/379823.

[10] Fanaroff, B. L. and Riley, J. M. 1974 "The morphology of extragalactic radio sources of high and low luminosity," *MNRAS* **167**, 31P-36P, DOI: 10.1093/mnras/167.1.31P.

[11] Fruscione, A., McDowell, J. C., Allen, G. E. et al. 2006 "CIAO: Chandra's data analysis system," in Silva, D. R. and Doxsey, R. E. eds. *Society of Photo-Optical Instrumentation Engineers (SPIE) Conference Series*, Society of Photo-Optical Instrumentation Engineers (SPIE) Conference Series.

[12] Garmire, G. P., Bautz, M. W., Ford, P. G., Nousek, J. A., and Ricker, J., George R. 2003 "Advanced CCD imaging spectrometer (ACIS) instrument on the Chandra X-ray Observatory," in Truemper, J. E. and Tananbaum, H. D. eds. *X-Ray and Gamma-Ray Telescopes and Instruments for Astronomy.*, Society of Photo-Optical Instrumentation Engineers (SPIE) Conference Series.

[13] Grandi, P., Guainazzi, M., Maraschi, L., Morganti, R., Fusco-Femiano, R., Fiocchi, M., Ballo, L., and Tavecchio, F. 2003 "Detection of X-Ray Emission from the Eastern Radio Lobe of Pictor A," *ApJ* **586**, No. 1, 123-127, DOI: 10.1086/367604.

[14] Griffin, M. J., Abergel, A., Abreu, A. et al. 2010 "The Herschel-SPIRE instrument and its in-flight performance," *A&A* **518**, L3, DOI: 10.1051/0004-6361/201014519.

[15] Hardcastle, M. J., Harris, D. E., Worrall, D. M., and Birkinshaw, M. 2004 "The Origins of X-Ray Emission from the Hot Spots of FR II Radio Sources," *ApJ* **612**, No. 2, 729-748, DOI: 10.1086/422808.

[16] Hardcastle, M. J., Croston, J. H., and Kraft, R. P. 2007 "A Chandra Study of Particle Acceleration in the Multiple Hot Spots of Nearby Radio Galaxies," *ApJ* **669**, No. 2, 893-904, DOI: 10.1086/521696.

[17] Hardcastle, M. J., Lenc, E., Birkinshaw, M. et al. 2016 "Deep Chandra observations of Pictor A," *MNRAS* **455**, No. 4, 3526-3545, DOI: 10.1093/mnras/stv2553.

[18] Harp, D. I., Liebe, C. C., Craig, W., Harrison, F., Kruse-Madsen, K., and Zoglauer, A. 2010 "NuSTAR: system engineering and modeling challenges in pointing reconstruction for a deployable x-ray telescope," in Angeli, G. Z. and Dierickx, P. eds. *Modeling, Systems Engineering, and Project Management for Astronomy IV*, Society of Photo-Optical Instrumentation Engineers (SPIE) Conference Series.

[19] Harris, D. E., Carilli, C. L., and Perley, R. A. 1994 "X-ray emission from the radio hotspots of Cygnus A," *Nature* **367**, No. 6465, 713-716, DOI: 10.1038/367713a0.

[20] Harris, D. E., Nulsen, P. E. J., Ponman, T. J. et al. 2000 "Chandra X-Ray Detection of the Radio Hot Spots of 3C 295," *ApJ* **530**, No. 2, L81-L84, DOI: 10.1086/312503.

[21] Harrison, F. A., Craig, W. W., Christensen, F. E. et al. 2013 "The Nuclear Spectroscopic Telescope Array (NuSTAR) High-energy X-Ray Mission," *ApJ* **770**, No. 2, 103, DOI: 10.1088/0004-637X/770/2/103.

[22] Heavens, A. F. and Meisenheimer, K. 1987 "Particle acceleration in extragalactic sources : the role of synchrotron losses in determining the spectrum.," *MNRAS* **225**, 335-353, DOI: 10.1093/mnras/225.2.335.

[23] Helder, E. A., Vink, J., Bykov, A. M., Ohira, Y., Raymond, J. C., and Terrier, R. 2012 "Observational Signatures of Particle Acceleration in Supernova Remnants," *Space Sci. Rev.* **173**, No. 1-4, 369-431, DOI: 10.1007/s11214-012-9919-8.

[24] HI4PI Collaboration, Ben Bekhti, N., Flöer, L. et al. 2016 "HI4PI: A full-sky H I survey based on EBHIS and GASS," *A&A* **594**, A116, DOI: 10.1051/0004-6361/201629178.

[25] Hillas, A. M. 1984 "The Origin of Ultra-High-Energy Cosmic Rays," *ARA&A* **22**, 425-444, DOI: 10.1146/annurev.aa.22.090184.002233.

[26] Inoue, S. and Takahara, F. 1996 "Electron Acceleration and Gamma-Ray Emission from Blazars," *ApJ* **463**, 555, DOI: 10.1086/177270.

[27] Isobe, N., Koyama, S., Kino, M., Wada, T., Nakagawa, T., Matsuhara, H., Niinuma, K., and Tashiro, M. 2017 "Mid-infrared Excess from the West Hot Spot of the Radio Galaxy Pictor A Unveiled by WISE," *ApJ* **850**, No. 2, 193, DOI: 10.3847/1538-4357/aa94c9.

[28] Isobe, N., Sunada, Y., Kino, M., Koyama, S., Tashiro, M., Nagai, H., and Pearson, C. 2020 "Herschel SPIRE Discovery of Far-infrared Excess Synchrotron Emission from the West Hot Spot of the Radio Galaxy Pictor A," *ApJ* **899**, No. 1, 17, DOI: 10.3847/1538-4357/ab9d1c.

[29] Ito, H., Kino, M., Kawakatu, N., Isobe, N., and Yamada, S. 2008 "The Estimate of Kinetic Power of Jets in FR II Radio Galaxies: Existence of Invisible Components?," *ApJ* **685**, No. 2, 828-838, DOI: 10.1086/591036.

[30] Jansen, F., Lumb, D., Altieri, B. et al. 2001 "XMM-Newton observatory. I. The spacecraft and operations," *A&A* **365**, L1-L6, DOI: 10.1051/0004-6361:20000036.

[31] Kang, J., Wang, J., and Kang, W. 2020 "NuSTAR Hard X-Ray Spectra of Radio Galaxies," *ApJ* **901**, No. 2, 111, DOI: 10.3847/1538-4357/abadf5.

[32] Kataoka, J., Mattox, J. R., Quinn, J. et al. 1999 "High-Energy Emission from the TEV Blazar Markarian 501 during Multiwavelength Observations in 1996," *ApJ* **514**, No. 1, 138-147, DOI: 10.1086/306918.

[33] Kataoka, J., Takahashi, T., Makino, F., Inoue, S., Madejski, G. M., Tashiro, M., Urry, C. M., and Kubo, H. 2000 "Variability Pattern and the Spectral Evolution of the BL Lacertae Object PKS 2155-304," *ApJ* **528**, No. 1, 243-253, DOI: 10.1086/308154.

[34] Kataoka, J. and Stawarz, Ł. 2005 "X-Ray Emission Properties of Large-Scale Jets, Hot Spots, and Lobes in Active Galactic Nuclei," *ApJ* **622**, No. 2, 797-810, DOI: 10.1086/428083.

[35] Kino, M. and Kawakatu, N. 2005 "Estimate of the total kinetic power and age of an extragalactic jet by its cocoon dynamics: the case of Cygnus A," *MNRAS* **364**, No. 2, 659-664, DOI: 10.1111/j.1365-2966.2005.09580.x.

[36] Kino, M. and Takahara, F. 2004 "Constraints on the energetics and plasma composition of relativistic jets in FR II sources," *MNRAS* **349**, 336-346, DOI: 10.1111/j.1365-2966.2004.07511.x.

[37] Kino, M., Kawakatu, N., and Takahara, F. 2012 "Calorimetry of Active Galactic Nucleus Jets: Testing Plasma Composition in Cygnus A," *ApJ* **751**, No. 2, 101, DOI: 10.1088/0004-637X/751/2/101.

[38] Kino, M., Takahara, F., and Kusunose, M. 2002 "Energetics of TeV Blazars and Physical Constraints on Their Emission Regions," *ApJ* **564**, No. 1, 97-107, DOI: 10.1086/323363.

[39] Kirk, J. G. and Duffy, P. 1999 "TOPICAL REVIEW: Particle acceleration and relativistic shocks," *Journal of Physics G Nuclear Physics* **25**, No. 8, R163-R194, DOI: 10.1088/0954-3899/25/8/201.

[40] Kirsch, M. G. F., Altieri, B., Chen, B. et al. 2004 "XMM-Newton (cross)-calibration," in Hasinger, G. and Turner, M. J. L. eds. *UV and Gamma-Ray Space Telescope Systems*, Society of Photo-Optical Instrumentation Engineers (SPIE) Conference Series.

[41] Kotera, K. and Olinto, A. V. 2011 "The Astrophysics of Ultrahigh-Energy Cosmic Rays," *ARA&A* **49**, No. 1, 119-153, DOI: 10.1146/annurev-astro-081710-102620.

[42] Kraft, R. P., Birkinshaw, M., Hardcastle, M. J., Evans, D. A., Croston, J. H., Worrall, D. M., and Murray, S. S. 2007 "A Radio through X-Ray Study of the Hot Spots, Active Nucleus, and Environment of the Nearby FR II Radio Galaxy 3C 33," *ApJ* **659**, No. 2, 1008-1021, DOI: 10.1086/512766.

[43] Lazio, T. J. W., Cohen, A. S., Kassim, N. E., Perley, R. A., Erickson, W. C., Carilli, C. L., and Crane, P. C. 2006 "Cygnus A: A Long-Wavelength Resolution of the Hot Spots," *ApJ* **642**, No. 1, L33–L36, DOI: 10.1086/504408.

[44] Mack, K. H., Prieto, M. A., Brunetti, G., and Orienti, M. 2009 "Near-infrared/optical counterparts of hotspots in radio galaxies," *MNRAS* **392**, No. 2, 705-717, DOI: 10.1111/j.1365-2966.2008.14081.x.

[45] MAGIC Collaboration, Acciari, V. A., Ansoldi, S. et al. 2020 "Testing two-component models on very high-energy gamma-ray-emitting BL Lac objects," *A&A* **640**, A132, DOI: 10.1051/0004-6361/202037811.

[46] McKean, J. P., Godfrey, L. E. H., Vegetti, S. et al. 2016 "LOFAR imaging of Cygnus A - direct detection of a turnover in the hotspot radio spectra," *MNRAS* **463**, No. 3, 3143-3150, DOI: 10.1093/mnras/stw2105.

[47] Meisenheimer, K., Roser, H. J., Hiltner, P. R., Yates, M. G., Longair, M. S., Chini, R., and Perley, R. A. 1989 "The synchrotron spectra of radio hot spots.," *A&A* **219**, 63-86.

[48] Meisenheimer, K., Yates, M. G., and Roeser, H.-J. 1997 "The synchrotron spectra of radio hot spots. II. Infrared imaging.," *A&A* **325**, 57-73.

[49] Migliori, G., Orienti, M., Coccato, L., Brunetti, G., D'Ammando, F., Mack, K. H., and Prieto, M. A. 2020 "Particle acceleration in low-power hotspots: modelling the broad-band spectral energy distribution," *MNRAS* **495**, No. 2, 1593-1607, DOI: 10.1093/mnras/staa1214.

[50] Migliori, G., Grandi, P., Palumbo, G. G. C., Brunetti, G., and Stanghellini, C. 2007 "Radio Lobes of Pictor A: An X-Ray Spatially Resolved Study," *ApJ* **668**, No. 1, 203-208, DOI: 10.1086/520870.

[51] Nagayoshi, T., Bamba, A., Katsuda, S., and Terada, Y. 2021 "Detection of the hard X-ray non-thermal emission from Kepler's supernova remnant," *PASJ* **73**, No. 2, 302-312, DOI: 10.1093/pasj/psaa121.

[52] Nakazawa, K., Mori, K., Tsuru, T. G. et al. 2018 "The FORCE mission: science aim and instrument parameter for broadband x-ray imaging spectroscopy with good angular resolution," in den Herder, J.-W. A., Nikzad, S., and Nakazawa, K. eds. *Space Telescopes and Instrumentation 2018: Ultraviolet to Gamma Ray*, Society of Photo-Optical Instrumentation Engineers (SPIE) Conference Series.

[53] Orienti, M., Migliori, G., Brunetti, G., Nagai, H., D'Ammando, F., Mack, K. H., and Prieto, M. A. 2020 "Jansky VLA observations of synchrotron emitting optical hotspots of 3C 227 and 3C 445 radio galaxies," *MNRAS* **494**, No. 2, 2244-2253, DOI: 10.1093/mnras/staa777.

[54] Page, M. J., Brindle, C., Talavera, A. et al. 2012 "The XMM-Newton serendipitous ultraviolet source survey catalogue," *MNRAS* **426**, No. 2, 903-926, DOI: 10.1111/j.1365-2966.2012.21706.x.

[55] Perley, R. A., Dreher, J. W., and Cowan, J. J. 1984 "The jet and filaments in Cygnus A," *ApJ* **285**, L35-L38, DOI: 10.1086/184360.

[56] Perlman, E. S., Georganopoulos, M., May, E. M., and Kazanas, D. 2010 "Chandra Observations of the Radio Galaxy 3C 445 and the Hot Spot X-Ray Emission Mechanism," *ApJ* **708**, No. 1, 1-8, DOI: 10.1088/0004-637X/708/1/1.

[57] Pilbratt, G. L., Riedinger, J. R., Passvogel, T. et al. 2010 "Herschel Space Observatory. An ESA facility for far-infrared and submillimetre astronomy," *A&A* **518**, L1, DOI: 10.1051/0004-6361/201014759.

[58] Plucinsky, P. P., Bogdan, A., Marshall, H. L., and Tice, N. W. 2018 "The complicated evolution of the ACIS contamination layer over the mission life of the Chandra X-ray Observatory," in den Herder, J.-W. A., Nikzad, S., and Nakazawa, K. eds. *Space Telescopes and Instrumentation 2018: Ultraviolet to Gamma Ray*, Society of Photo-Optical Instrumentation Engineers (SPIE) Conference Series.

[59] Poglitsch, A., Waelkens, C., Geis, N. et al. 2010 "The Photodetector Array Camera and Spectrometer (PACS) on the Herschel Space Observatory," *A&A* **518**, L2, DOI: 10.1051/0004-6361/201014535.

[60] Predehl, P., Andritschke, R., Arefiev, V. et al. 2021 "The eROSITA X-ray telescope on SRG," *A&A* **647**, A1, DOI: 10.1051/0004-6361/202039313.

[61] Savage, R. S. and Oliver, S. 2007 "Bayesian Methods of Astronomical Source Extraction," *ApJ* **661**, No. 2, 1339-1346, DOI: 10.1086/515393.

[62] Snios, B., Nulsen, P. E. J., Wise, M. W. et al. 2018 "The Cocoon Shocks of Cygnus A: Pressures and Their Implications for the Jets and Lobes," *ApJ* **855**, No. 1, 71, DOI: 10.3847/1538-4357/aaaf1a.

[63] Spitkovsky, A. 2008 "Particle Acceleration in Relativistic Collisionless Shocks: Fermi Process at Last?," *ApJ* **682**, No. 1, L5, DOI: 10.1086/590248.

[64] Stawarz, Ł., Cheung, C. C., Harris, D. E., and Ostrowski, M. 2007 "The Electron Energy Distribution in the Hotspots of Cygnus A: Filling the Gap with the Spitzer Space Telescope," *ApJ* **662**, 213-223, DOI: 10.1086/517966.

[65] Strüder, L., Briel, U., Dennerl, K. et al. 2001 "The European Photon Imaging Camera on XMM-Newton: The pn-CCD camera," *A&A* **365**, L18-L26, DOI: 10.1051/0004-6361:20000066.

[66] Swinyard, B. M., Ade, P., Baluteau, J. P. et al. 2010 "In-flight calibration of the Herschel-SPIRE instrument," *A&A* **518**, L4, DOI: 10.1051/0004-6361/201014605.

[67] Thimmappa, R., Stawarz, Ł., Marchenko, V., Balasubramaniam, K., Cheung, C. C., and Siemiginowska, A. 2020 "Chandra Imaging of the Western Hotspot in the Radio Galaxy Pictor A: Image Deconvolution and Variability Analysis," *ApJ* **903**, No. 2, 109, DOI: 10.3847/1538-4357/abb605.

[68] Thomson, R. C., Crane, P., and Mackay, C. D. 1995 "Optical Structure and Polarization of the Western Hot SPOT of Pictor A," *ApJ* **446**, L93, DOI: 10.1086/187938.

[69] Tingay, S. J., Lenc, E., Brunetti, G., and Bondi, M. 2008 "A High Resolution View of the Jet Termination Shock in a Hot Spot of the Nearby Radio Galaxy Pictor A: Implications for X-Ray Models of Radio Galaxy Hot Spots," *AJ* **136**, No. 6, 2473-2482, DOI: 10.1088/0004-6256/136/6/2473.

[70] Turner, M. J. L., Abbey, A., Arnaud, M. et al. 2001 "The European Photon Imaging Camera on XMM-Newton: The MOS cameras," *A&A* **365**, L27-L35, DOI: 10.1051/0004-6361:20000087.

[71] Vink, J. 2012 "Supernova remnants: the X-ray perspective," *A&ARv* **20**, 49, DOI: 10.1007/s00159-011-0049-1.

[72] Weisskopf, M. C., Tananbaum, H. D., Van Speybroeck, L. P., and O'Dell, S. L. 2000 "Chandra X-ray Observatory (CXO): overview," in Truemper, J. E. and Aschenbach, B. eds. *X-Ray Optics, Instruments, and Missions III*, Society of Photo-Optical Instrumentation Engineers (SPIE) Conference Series.

[73] Werner, M. W., Murphy, D. W., Livingston, J. H., Gorjian, V., Jones, D. L., Meier, D. L., and Lawrence, C. R. 2012 "Spitzer Observations of Hotspots in Radio Lobes," *ApJ* **759**, No. 2, 86, DOI: 10.1088/0004-637X/759/2/86.

[74] Wilson, A. S., Young, A. J., and Shopbell, P. L. 2000 "Chandra Observations of Cygnus A: Magnetic Field Strengths in the Hot Spots of a Radio Galaxy," *ApJ* **544**, No. 1, L27-L30, DOI: 10.1086/317293.

[75] ——— 2001 "Chandra X-Ray Observations of Pictor A: High-Energy Cosmic Rays in a Radio Galaxy," *ApJ* **547**, No. 2, 740-753, DOI: 10.1086/318412.

[76] Wilson, A. S., Smith, D. A., and Young, A. J. 2006 "The Cavity of Cygnus A," *ApJ* **644**, No. 1, L9-L12, DOI: 10.1086/504108.

[77] Wright, M. C. H. and Birkinshaw, M. 2004 "The Hot Spots of Cygnus A at 230 GHz," *ApJ* **614**, 115-121, DOI: 10.1086/423483.

[78] Yaji, Y., Tashiro, M. S., Isobe, N., Kino, M., Asada, K., Nagai, H., Koyama, S., and Kusunose, M. 2010 "Evidence of Non-thermal X-ray Emission from Radio Lobes of Cygnus A," *ApJ* **714**, No. 1, 37-44, DOI: 10.1088/0004-637X/714/1/37.

[79] Zabalza, V. 2015 "Naima: a Python package for inference of particle distribution properties from nonthermal spectra," in *34th International Cosmic Ray Conference (ICRC2015)* **34** of International Cosmic Ray Conference, 922.

[80] Zhang, J., Du, S.-s., Guo, S.-C., Zhang, H.-M., Chen, L., Liang, E.-W., and Zhang, S.-N. 2018 "Examining the High-energy Radiation Mechanisms of Knots and Hotspots in Active Galactic Nucleus Jets," *ApJ* **858**, No. 1, 27, DOI: 10.3847/1538-4357/aab9b2.